Geophysical Journal International

Geophys. J. Int. (2012) **191,** 1325–1342 doi: 10.1111/j.1365-246X.2012.05679.x

Properties of inelastic yielding zones generated by in-plane dynamic ruptures—I. Model description and basic results

Shiqing Xu,[1] Yehuda Ben-Zion[1] and Jean-Paul Ampuero[2]

[1]*Department of Earth Sciences, University of Southern California, Los Angeles, CA, USA. E-mail: shiqingx@usc.edu*
[2]*Seismological Laboratory, California Institute of Technology, Pasadena, CA, USA*

Accepted 2012 September 13. Received 2012 July 4; in original form 2012 February 8

SUMMARY

We discuss results associated with 2-D numerical simulations of in-plane dynamic ruptures on a fault governed by slip-weakening and rate-and-state friction laws with off-fault yielding. The onset of yielding is determined by a Mohr–Coulomb-type criterion whereas the subsequent inelastic response is described by a Duvaut-Lions-type viscoplastic rheology. The study attempts to identify key parameters and conditions that control the spatial distribution and the intensity variation of off-fault yielding zones, the local orientation of the expected microfractures, and scaling relations or correlations among different quantities that can be used to characterize the yielding zones. In this paper, we present example results for crack and pulse ruptures, along with calculations of energy partition and characteristics of the simulated off-fault yielding zones. A companion follow-up paper provides a comprehensive parameter-space study of various examined features. In agreement with previous studies, the location and shape of the off-fault yielding zones depend strongly on the angle Ψ of the background maximum compressive stress relative to the fault and the crack versus pulse mode of rupture. Following initial transients associated with nucleation of ruptures, the rate of various energy components (including off-fault dissipation) linearly increases with time for cracks, while approaching a constant level for pulse-like ruptures. The local angle to the fault of the expected microfractures is generally shallower and steeper than Ψ in the compressional and extensional quadrants, respectively. The scalar seismic potency density decays logarithmically with increasing fault normal distance, with decay slope and maximum value that are influenced by the operating stress field.

Key words: Microstructures; Elasticity and anelasticity; Rheology and friction of fault zones; Dynamics and mechanics of faulting; Fractures and faults; Mechanics, theory, and modelling.

1 INTRODUCTION

Natural fault zones have an internal structure consisting of a core with one or several highly localized (e.g. cm-wide) slip zones that accommodate most of the fault motion, and surrounding damage zone with fractured and crushed rock products such as breccias and cataclasites (e.g. Ben-Zion & Sammis 2003, and references therein). In large faults, the damage zone has typically significant fracture density over hundred to several hundred metres and it then tapers to properties of the host rocks (e.g. Chester *et al.* 1993; Caine *et al.* 1996; Faulkner *et al.* 2003; Dor *et al.* 2008). Although the fault core plays the key role in the long-term deformation, characteristics of the broader damage zone contain important information on the stress conditions during failure and dynamic properties of earthquake ruptures (e.g. Wilson *et al.* 2003; Ben-Zion & Shi 2005; Dor *et al.* 2006a; Templeton & Rice 2008; Mitchell & Faulkner 2009; Dunham *et al.* 2011; Huang & Ampuero 2011).

Theoretical studies on off-fault yielding during rapid propagation of shear ruptures on a frictional fault have used analytical approaches and numerical simulations. Poliakov *et al.* (2002) and Rice *et al.* (2005) constructed, based on previous studies, non-singular crack and pulse models by balancing the stress intensity factor and the frictional resistance over a finite (process) zone behind the rupture tip. Both works examined properties of the elastically predicted off-fault secondary fractures by adopting the Mohr–Coulomb criterion. They found that the spatial pattern of potential yielding zones depends strongly on the orientation of the background stress field, the rupture speed, ratio of residual to peak stress, size of slipping patch and whether the rupture is in-plane or antiplane. For mode-II in-plane ruptures, which are the focus of our study, the extent of the off-fault zones predicted to yield increases considerably with increasing rupture speed close to the limiting subsonic values. The inferred dynamic stress orientation inside the potential yielding zones can be significantly altered from the background and

residual levels (with a possible reversed sign of shear component) when the ratio of residual to peak stress is small and the rupture speed approaches the Rayleigh wave speed.

Yamashita (2000) and Dalguer *et al.* (2003) used, respectively, stress- and fracture-energy-based criteria to model the formation of discretely distributed off-fault tensile microfractures. Ando & Yamashita (2007) assumed a hoop shear maximization criterion to model the formation of shear branches nucleated by a propagating rupture at a series of prescribed points along the fault. Andrews (2005), Ben-Zion & Shi (2005), Duan (2008), Ma & Andrews (2010) and others used Mohr–Coulomb or Drucker–Prager-type criteria to model dynamic off-fault yielding as continuously distributed plastic strain over the surrounding bulk. These studies represented situations corresponding to large strike-slip faults by assuming that the angle between the background maximum compressive stress and the fault is $\Psi = 45^\circ$, and found that the off-fault yielding is generated primarily on the extensional sides of the faults. Ben-Zion & Shi (2005) noted that the shape of the off-fault yielding zone for crack-like ruptures is triangular, whereas for steady-state pulse-like ruptures it is approximately constant, owing to the different stress concentrations in these two rupture styles: expanding cracks (or expanding pulses) have increasing size of slipping zone and increasing stress concentration, whereas steady-state pulses have approximately constant slipping zone and stress concentrations. Templeton & Rice (2008) and Dunham *et al.* (2011) performed systematic numerical simulations of off-fault plastic yielding for different values of Ψ and confirmed the theoretical expectations of Poliakov *et al.* (2002) and Rice *et al.* (2005): the plastic yielding zone is primarily in the compressional and extensional quadrants when $\Psi < 20^\circ$ and $\Psi > 30^\circ$, respectively.

The properties of distributed off-fault yielding zones have been examined in various field studies, believed to be closely related to propagation of dynamic ruptures along approximately planar surfaces, and laboratory experiments. Di Toro *et al.* (2005) documented quasi-periodic arrays of pseudo-tachylyte injection veins that are mainly on the extensional side, and at high angles (sometimes almost orthogonal), relative to the Gole Larghe fault in the Italian Alps. Rousseau & Rosakis (2003, 2009), Griffith *et al.* (2009) and Ngo *et al.* (2012) observed in laboratory experiments of dynamic ruptures along a glued interface between two Homalite samples arrays of tensile microfractures that are quasi-periodically distributed along the rupture path, at certain angles relative to the interface, depending on the loading conditions and rupture speed. The spatial distribution and local orientation of both pseudo-tachylyte injection veins in the field and tensile microfractures generated in labs can be well explained by theoretical analysis based on linear elastic fracture mechanics (LEFM) or other non-singular fault models emphasizing the dynamic effects of a rapidly propagating rupture near its tip (e.g. Di Toro *et al.* 2005; Ngo *et al.* 2012).

Various studies examined the interaction between dynamic ruptures and properties of the bounding host rocks. During propagation of in-plane ruptures along a bimaterial interface separating different elastic solids, there is a coupling between slip and dynamic changes of normal stress (σ_n) that does not exist in a homogeneous solid (e.g. Weertman 1980; Andrews & Ben-Zion 1997; Ben-Zion 2001). For subshear ruptures the change of σ_n at the tip propagating in the direction of particle motion in the compliant solid (referred to as the positive direction) is tensile, whereas the change at the tip propagating in the opposite direction is compressive. The amplitudes of the dynamic changes of σ_n near the rupture tips increase with propagation distance because of continual transfer of energy to shorter wavelengths (e.g. Adams 1995; Ranjith & Rice 2001; Ben-Zion & Huang 2002; Rubin & Ampuero 2007). The increase in the along-strike asymmetry of the dynamic bimaterial effects with propagation distance leads for various conditions (e.g. Ben-Zion & Andrews 1998; Shi & Ben-Zion 2006; Ampuero & Ben-Zion 2008; Brietzke *et al.* 2009; Dalguer & Day 2009) to the development of pulses propagating in the positive direction with strong reduction of normal stress near the propagating tip.

Ben-Zion & Shi (2005) simulated dynamic ruptures on a bimaterial interface with constant friction coefficient, off-fault Coulomb plastic yielding and $\Psi = 45^\circ$. In various cases associated with different sets of initial stress values, degree of material contrast and rock cohesion, ruptures evolved quickly to unilateral pulses in the positive direction and off-fault yielding occurred primarily in a strip of approximately constant thickness in the extensional quadrant. They proposed that the cumulative effect of multiple such ruptures would produce a strong asymmetry in the distribution of off-fault yielding zones, with most yielding on the side with higher seismic velocity at seismogenic depth. Rubin & Ampuero (2007) suggested from simulations of bimaterial ruptures with slip-weakening friction (SWF) that asymmetric off-fault yielding may occur also for bilateral cracks, because of the strong asymmetry of the dynamic stress fields near the crack tips propagating in the opposite directions. Duan (2008) obtained asymmetric yielding in simulations of bilateral crack ruptures on a bimaterial interface with SWF, off-fault plasticity and $\Psi = 45^\circ$. However, using in such cases low cohesion representing situations close to the free surface produced significant inelastic strain in both propagation directions. Ampuero & Ben-Zion (2008) showed that with velocity-dependent friction, the feedback between the asymmetric dynamic slip rates and stress drops near the different rupture tips leads to the development of macroscopically asymmetric ruptures.

Dor *et al.* (2006a,b 2008), Wechsler *et al.* (2009) and Mitchell *et al.* (2011) observed with geological mapping and remote sensing data strongly asymmetric damage zones across sections of the San Andreas and San Jacinto faults in southern California, the North Anatolian fault in Turkey and the Arima-Takatsuki Tectonic Line in Japan. Lewis *et al.* (2005, 2007) observed with seismic trapped and head waves asymmetric damage zones across sections of the San Jacinto and San Andreas faults. These studies documented with multiple signals damage asymmetry in features of fault structures over length scales ranging from centimetres to several kilometres. In all examined places, considerable more damage was present on the sides of the faults having, based on seismic imaging and laboratory measurements, faster seismic velocities at depth.

DeDontney *et al.* (2011) performed detailed simulations of yielding patterns during propagation of in-plane bimaterial ruptures associated with different values of Ψ. They found, in agreement with previous studies, that the pattern of the simulated yielding zones depends strongly on Ψ, and that for cases with sufficiently shallow Ψ, for which the yielding is primarily on the compressional side, the preferred rupture propagation is in the negative direction. Rudnicki & Rice (2006), Dunham & Rice (2008) and Viesca *et al.* (2008) considered interactions between dynamic ruptures and contrasts of poroelasticity or permeability inside and outside the fault zones. These fault zone ingredients are not considered in our work.

In this study we attempt to characterize various properties of yielding zones around faults generated spontaneously by dynamic in-plane ruptures with different frictional responses, variable initial stress conditions and rock cohesion values, possible existence of elasticity contrast across the fault, and conditions representing different depth sections. The results are presented in two related papers. In this first paper, we describe various components of the

model and show example simulation results associated with crack- and pulse-type ruptures in a homogenous solid. The results are used to verify the consistency of the computations, through examination of the conservation and partition of energy during propagation of ruptures and to define quantities that can be used to characterize off-fault yielding zones. These include the location, shape and intensity of the yielding patterns, the local orientation of expected microfractures, the decay of yielding density with normal distance from the fault, and possible scaling relations or correlations among different measurable quantities. In the second companion paper, we present a systematic study of effects associated with various model parameters. The results of both papers help to develop improved quantitative connections between mechanics and field observations of earthquake faults.

2 MODEL SET-UP

We aim to numerically simulate dynamic in-plane ruptures and the spontaneous generation of off-fault yielding along strike-slip faults. For a 3-D problem with plane strain assumption, the stress field is represented by

$$\sigma_{ij} = \begin{bmatrix} \sigma_{xx} & \sigma_{xy} & 0 \\ \sigma_{yx} & \sigma_{yy} & 0 \\ 0 & 0 & \sigma_{zz} \end{bmatrix}, \tag{1}$$

with no motion or deformation along the z-axis ($u_z = 0, \partial/\partial z = 0$). During the considered in-plane ruptures (Fig. 1) the stress components of primary interest are σ_{xx}, $\sigma_{xy} = \sigma_{yx}$ and σ_{yy}, whereas the stress component σ_{zz} evolves with changing plane strain components ε_{xx} and ε_{yy}. According to Anderson's theory for strike-slip faulting, the intermediate principal stress σ_{int} coincides with σ_{zz}, whereas the maximum principal stress σ_{max} (compressive in the Earth's crust) and the minimum σ_{min} (which is usually compressive but can become tensile) are in the $x - y$ plane. The orientation and relative magnitude of σ_{max} and σ_{min} determine the partition of different stress components (or vice versa; e.g. Scholz 2002). In our 2-D simulations, right-lateral rupture is nucleated in a prescribed zone (marked with red colour in Fig. 1) and then is allowed to spontaneously propagate along the frictional fault (black solid line in Fig. 1). The initial normal and shear stresses on the fault and surrounding medium are $\sigma_0 = \sigma^0_{yy}$ and $\tau_0 = \sigma^0_{xy}$.

The relative strength S parameter, defined by

$$S = \frac{\tau_s - \tau_0}{\tau_0 - \tau_d}, \tag{2}$$

is often used to describe the relative closeness of the initial shear stress to the static yielding level (Andrews 1976; Das & Aki 1977). Here $\tau_s = f_s(-\sigma_0)$ (negative sign for compressive normal stress) is the static shear strength (giving the peak shear stress level) and $\tau_d = f_d(-\sigma_0)$ is the dynamic shear strength (giving the residual stress level under sliding), with f_s and f_d being the static and dynamic friction coefficient, respectively. In our all simulations, S is set at a relatively high level such that ruptures are in the subshear regime (e.g. for crack-like ruptures, $S > 1.77$).

The acute angle between the maximum compressive stress and the fault plane is denoted Ψ. The initial stress state can be expressed in terms of Ψ, S and remote loading (Fig. 1) as

$$\sigma^0_{xy} = \frac{f_s + S f_d}{1 + S}\left(-\sigma^0_{yy}\right), \tag{3}$$

$$\sigma^0_{xx} = \left[1 - \frac{2\sigma^0_{xy}}{\tan(2\Psi)\,\sigma^0_{yy}}\right]\sigma^0_{yy}, \tag{4}$$

with fixed friction coefficients $f_s = 0.6$ and $f_d = 0.1$, we can change S and Ψ to assign initial values to σ^0_{xy} and σ^0_{xx} (e.g. Templeton & Rice 2008). Once the rupture starts to propagate, the total stress field is the sum of the initial state and the slip-induced increment. A nominal dynamic value of Ψ can be inferred by:

$$\Psi = \frac{1}{2}\arccos\left[\frac{\sigma_{yy} - \sigma_{xx}}{\sqrt{(\sigma_{yy} - \sigma_{xx})^2 + 4\sigma^2_{xy}}}\right]\text{sgn}(\sigma_{xy}), \tag{5}$$

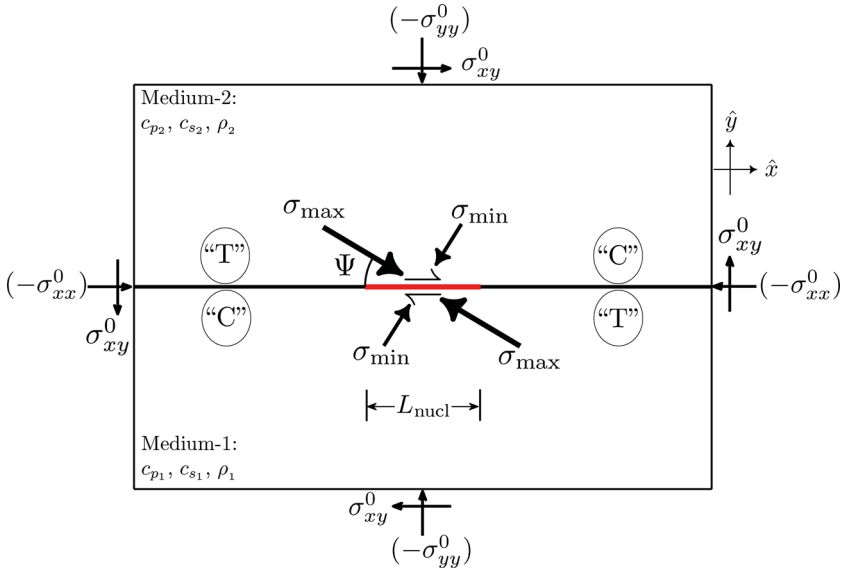

Figure 1. A 2-D model configuration of in-plane rupture along a planar frictional interface. The medium is loaded by a uniform background stress state with angle Ψ of the maximum compressive stress σ_{max} relative to the fault. Symbols 'C' and 'T' represent the compressional and extensional quadrants in relation to the first motion of P waves from the nucleation zone. In simulations incorporating a material contrast across the fault, medium-1 and medium-2 are the stiff and compliant sides, respectively.

where Ψ is still defined as the acute angle between the maximum compressive stress and fault plane, and sgn$(\cdot)$ is the sign function accounting for a possibility that the sign of shear stress σ_{xy} can be temporarily reversed by the dynamic effect of a rapidly propagating rupture (this is illustrated in the later Figs 11 and 12).

To allow a possible material contrast across the fault, a subscript 'i' is used to represent the Lamé parameters λ_i, μ_i and mass density ρ_i in the lower stiff medium ($i = 1$) and the upper compliant medium ($i = 2$). Following the convention used by Ben-Zion & Shi (2005) and Shi & Ben-Zion (2006), we adopt a non-dimensional number $\gamma \geq 0$ to quantify the degree of material contrast as $1 + \gamma = c_{p1}/c_{p2} = c_{s1}/c_{s2} = \rho_1/\rho_2$ (with the same Poisson's ratio ν for both sides), where $c_{pi} = \sqrt{(\lambda_i + 2\mu_i)/\rho_i}$ and $c_{si} = \sqrt{\mu_i/\rho_i}$ are the P- and S-wave speeds in the 'ith' medium, respectively.

2.1 Friction laws

Slip occurs when the on-fault shear stress reaches the frictional strength: $\tau = f(-\sigma)$, where f is the friction coefficient and $(-\sigma)$ is the effective normal stress. To study off-fault plastic response under different rupture styles, both SWF and rate-and-state friction (RSF) with fast weakening are employed to produce crack-like and pulse-like ruptures, respectively.

2.1.1 Linear SWF

SWF laws (e.g. Ida 1972; Palmer & Rice 1973; Andrews 1976) have been widely applied to model a single earthquake rupture process as an expanding crack. The concept of a process zone where strength degradation spatially occurs, also called cohesive zone or breakdown zone (e.g. Ben-Zion 2003), eliminates the stress singularity around the rupture tip and provides a spatial requirement for numerical resolution (e.g. Rice 1980; Day *et al.* 2005). In our simulations, a simple form is adopted where the friction coefficient linearly decreases as a function of slip from its static value to the dynamic level:

$$f = \begin{cases} f_s - (f_s - f_d)\,\Delta u/D_c & \text{if} \quad \Delta u \leq D_c \\ f_d & \text{if} \quad \Delta u > D_c \end{cases}, \tag{6}$$

where D_c is the characteristic slip distance for the degradation of the friction coefficient (Fig. 2). When the background shear stress is only slightly greater than the dynamic shear strength $\tau_d = f_d(-\sigma)$, the size of the process zone R can be estimated (Palmer & Rice 1973) by

$$R = \frac{R_0}{f_{\rm II}(v_r)}. \tag{7}$$

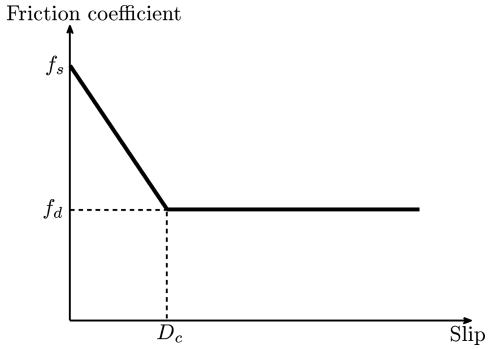

Figure 2. A linear slip-weakening friction law used to produce spontaneously propagating crack-like ruptures outside the nucleation zone. D_c is a characteristic slip distance for the reduction of the friction coefficient.

Here R_0 is the static value of R at zero rupture speed expressed as

$$R_0 = \frac{9\pi}{32(1-\nu)}\frac{\mu D_c}{|\sigma|\,(f_s - f_d)}, \tag{8}$$

and $f_{\rm II}(v_r)$ is a universal function of the rupture speed v_r expressed as

$$f_{\rm II}(v_r) = \frac{\alpha_s\left(1-\alpha_s^2\right)}{(1-\nu)\left[4\alpha_p\alpha_s - (1+\alpha_s^2)^2\right]}, \tag{9}$$

with $\alpha_p = \sqrt{1 - v_r^2/c_p^2}$ and $\alpha_s = \sqrt{1 - v_r^2/c_s^2}$. The function $f_{\rm II}(v_r)$ is often identified with the Lorentz contraction effect, because the size of the process zone R shrinks from R_0 to zero as v_r increases from 0^+ to the limiting speed. In a homogeneous solid, the latter is the Rayleigh wave speed c_R for mode-II ruptures. When there is a material contrast across the fault, the limiting speed is (for the range of material contrast in our study) the generalized Rayleigh wave speed c_{GR} (e.g. Weertman 1980; Ben-Zion 2001). The associated length scale R' has been estimated by Rubin & Ampuero (2007) using the same friction law as

$$R' = \frac{\bar{\mu}}{\mu'}R_0' = \frac{9\pi\bar{\mu}D_c}{32\Delta\tau}, \tag{10}$$

where $\bar{\mu}$ is a function of the material properties and rupture speed v_r (Weertman 1980), $\mu' \equiv \bar{\mu}_0$ is an effective static modulus of the bimaterial solid (Rubin & Ampuero 2007; eq. A8), R_0' is the static value of R' and $\Delta\tau$ is the stress drop over R'.

2.1.2 Rate- and state-dependent friction

Laboratory studies indicate that rock friction depends not only on slip, but also on slip rate and properties of the contact area (e.g. Dieterich 1979, 1981; Rice & Ruina 1983; Ruina 1983; Marone 1998). Moreover, seismic observations suggest earthquakes may rupture not necessarily as cracks but as narrow slip pulses (e.g. Heaton 1990). Different mechanisms, with and without friction-dominant effects, have been proposed to produce pulse-like ruptures (Ben-Zion 2001, and references therein). In our study, we follow Ampuero & Ben-Zion (2008) and produce pulse-type ruptures using the following RSF law with fast weakening:

$$f = f_s + a\frac{V}{V + V_c} - b\frac{\theta}{\theta + D_c}, \tag{11}$$

where V_c and D_c are characteristic slip velocity and slip distance (Fig. 3). The response of the above friction to slip velocity consists

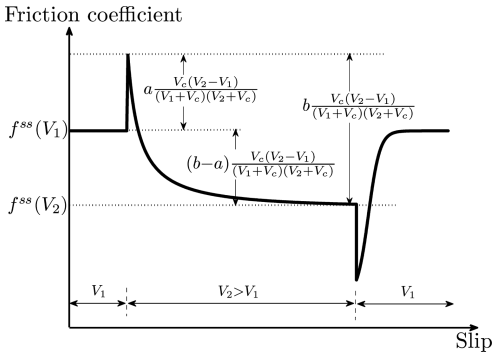

Figure 3. A rate- and state-dependent friction law used with velocity-weakening parameters ($a < b$) to produce spontaneously propagating pulse-like ruptures outside the nucleation zone. $f_{ss}(V)$ is the steady-state value of friction coefficient under a constant slip velocity V.

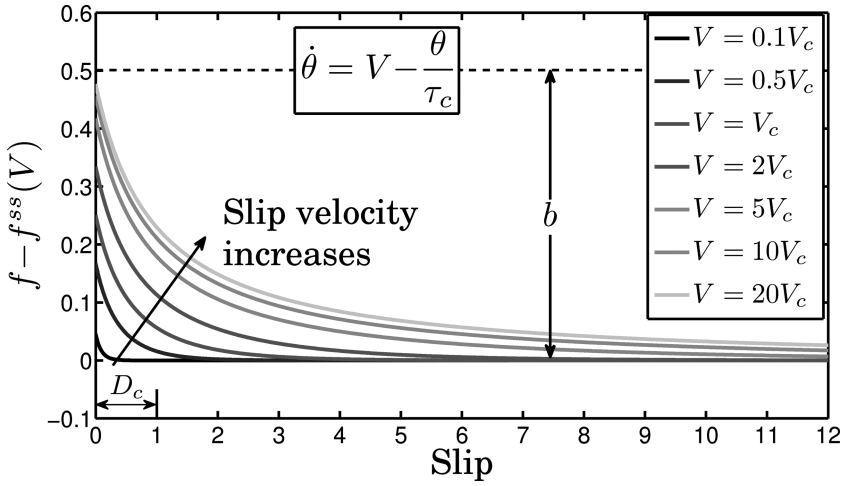

Figure 4. Effective slip-weakening distance D_c^{eff} for rate- and state-dependent friction with a step-like velocity jump from 0 to a constant value V (in steady state). Associated with an 'aging law' for the evolution of the state variable θ, D_c^{eff} generally increases with the steady-state value of V.

of two competing effects. The a term has a velocity-strengthening mechanism with an instantaneous (direct) response to the change of slip velocity V. The b term has a velocity-weakening response to the change of V through an evolution (indirect) process, described by a state variable θ:

$$\dot{\theta} = V - \frac{\theta}{\tau_c}, \tag{12}$$

where $\tau_c = D_c/V_c$ is a characteristic timescale over which friction evolves towards steady state in the current slip velocity regime V^{ss}:

$$f^{ss} = f_s + (a-b)\frac{V^{ss}}{V^{ss}+V_c}. \tag{13}$$

We set $(a-b) < 0$ so the friction in steady state is effectively velocity weakening, which decays as $1/V$ towards a nominal dynamic level $f_d = f_s + (a-b)$ for $V \gg V_c$. Because of the dependence of friction on V, the effective slip-weakening distance D_c^{eff} is not a constant. With a sudden jump of V from zero to a steady state value of V^{ss}, D_c^{eff} increases with V^{ss} (Fig. 4). This trend is in general consistent with previous studies adopting an aging law for the state variable θ (e.g. Cocco & Bizzarri 2002; Ampuero & Rubin 2008), though the specific scaling relation between D_c^{eff} and V^{ss} depends on details of the friction laws.

The above state variable used in our study (θ) is related to that of Ampuero & Ben-Zion (2008) (θ') through a unit conversion, $\theta = \theta'\tau_c$. Therefore, similar analysis on rupture-style transition can be performed by studying the characteristic healing timescale τ_c: a rupture pulse is expected to be produced for $\tau_c \ll \theta/\dot{\theta}$ (dominance of velocity-weakening behaviour, $\theta \approx V\tau_c$) whereas a crack is expected for $\tau_c \gg \theta/\dot{\theta}$ (dominance of slip-weakening behaviour, $\dot{\theta} \approx V$). Because the behaviour of the friction coefficient in steady state has the same dependence on slip velocity as in Ampuero & Ben-Zion (2008), we can follow the analysis in appendix A of that paper. This provides a critical wavelength to be well resolved within a homogeneous medium:

$$\lambda_{\text{cr}} \approx \frac{\pi\mu D_c}{(1-\nu)(b-a)|\sigma|}\frac{1}{\sqrt{1+(V_c/V_{\text{dyn}})^2}}, \tag{14}$$

with

$$V_{\text{dyn}} = \frac{(1-\nu)(b-a)|\sigma|}{\mu/2c_R}\sqrt{\frac{a}{b-a}}. \tag{15}$$

For a bimaterial fault, the equivalent critical wavelength might be expressed as:

$$\lambda'_{\text{cr}} \approx \frac{\pi\mu' D_c}{(b-a)|\sigma'|}\frac{1}{\sqrt{1+(V_c/V'_{\text{dyn}})^2}}, \tag{16}$$

where μ' is the effective modulus which has been discussed for SWF, σ' is the effective normal stress along the bimaterial interface and V'_{dyn} is the corresponding version of eq. (A5) in Ampuero & Ben-Zion (2008) with the replacement of $(1-\nu)/\mu$ by $1/\mu'$, σ by σ' and c_R by c_{GR} (c_{GR} always exists in our study).

2.2 Nucleation procedure

We use a time-weakening friction (TWF) (e.g. Andrews 1985; Bizzarri 2010) with a uniform initial stress to artificially nucleate the rupture in a prescribed zone I_{nucl}, during a certain time period $[0, t_{\text{nucl}}]$:

$$f = \begin{cases} \min\{f^{\text{PHY}}, f^{\text{TWF}}\}, & \forall\{x, y, t\} \in I_{\text{nucl}} \times [0, t_{\text{nucl}}] \\ f^{\text{PHY}}, & \text{otherwise} \end{cases}. \tag{17}$$

The actual friction coefficient that governs the fault is chosen to be the minimum of the TWF f^{TWF} and the physical friction f^{PHY} during the nucleation time period ($0 \le t \le t_{\text{nucl}}$) for regions inside the zone I_{nucl}. For regions outside I_{nucl} during the nucleation time period, and for the entire fault beyond that period, the physical friction f^{PHY} determines how the friction coefficient evolves. The physical friction f^{PHY} has the form defined by eq. (6) (f^{SWF}) or by eq. (11) (f^{RSF}). The prescribed TWF f^{TWF} within the nucleation time period is defined as:

$$f^{\text{TWF}} = \min\left\{\max\left\{f_0 - \frac{(f_s - f_d)(v_r t - r)}{L_0}, f_d\right\}, f_s\right\}, \tag{18}$$

where $f_0 = \tau_0/(-\sigma_0)$, $r = \sqrt{(x-x_0)^2 + (y-y_0)^2}$ is the distance from the hypocentre $\{x_0, y_0\}$ and v_r is the prescribed subshear rupture speed ($v_r = 0.75c_s$). From the above definition, the friction coefficient linearly decreases at a fixed time from its static level f_s at the rupture front to the dynamic level f_d over a characteristic length scale L_0 behind the rupture front and is low bounded by f_d (Fig. 5, left). At a fixed point, the friction coefficient weakens with time and is also low bounded by f_d (Fig. 5, right). The size of the

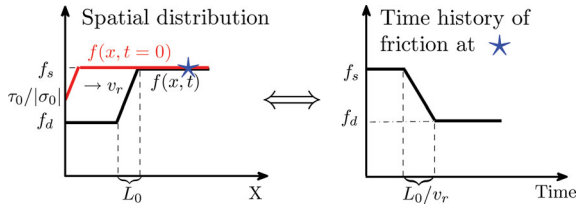

Figure 5. Time-weakening friction law adopted to artificially nucleate the rupture. (Left) Spatial distribution of friction coefficient along strike. (Right) Time history of friction coefficient at a fixed point. L_0 is a characteristic length scale for the reduction of friction coefficient and v_r is a prescribed outward-propagating rupture speed.

nucleation zone is determined by the prescribed rupture speed and desired time duration t_{nucl}, which in practice is chosen to be large enough such that the subsequent spontaneous rupture can propagate over a long distance along the fault.

2.3 Normal stress response

The Prakash–Clifton regularization of the normal stress response, as required for bimaterial rupture problems (e.g. Cochard & Rice 2000; Ben-Zion & Huang 2002), is used in the form proposed by Rubin & Ampuero (2007). Specifically, the fault strength $\tau = f \cdot \max\{0, -\sigma^*\}$ is proportional to a modified normal stress σ^* (if it remains compressive, otherwise fault opening will be produced by setting $\sigma^* = 0$), with some time delay in response to abrupt change of the actual fault normal stress σ:

$$\dot{\sigma}^* = \frac{|V| + V^*}{\delta_c}(\sigma - \sigma^*), \tag{19}$$

where V^* is a reference slip velocity and δ_c is a characteristic slip distance. As noted by Rubin & Ampuero (2007), the adopted form of σ^* in eq. (19) evolves with both time and slip. This can produce a prominent bimaterial effect if the evolution of σ^* near the rupture front is rapid compared to that of the friction coefficient. In our study, V^* is chosen to be comparable with the expected peak slip velocity near the rupture front and δ_c is set to be a moderate fraction of D_c (e.g. $\delta_c = 0.6D_c$) such that the potential bimaterial effect is neither suppressed nor overly emphasized.

2.4 Off-fault plastic response

Following Andrews (2005), Ben-Zion & Shi (2005) and later works, the Mohr–Coulomb criterion is adopted in our 2-D study for the onset of off-fault yielding. With this, yielding occurs when the maximum shear stress over all orientations,

$$\tau_{\max} = \sqrt{\sigma_{xy}^2 + (\sigma_{xx} - \sigma_{yy})^2/4}, \tag{20}$$

exceeds a pressure-dependent yielding strength

$$\sigma_Y = c\cos(\phi) - \sigma_m \sin(\phi), \tag{21}$$

where c is the rock cohesion, ϕ is the internal friction angle and $\sigma_m = (\sigma_{xx} + \sigma_{yy})/2$ is the mean stress (Fig. 6). The above criterion may be alternatively expressed by a yielding function

$$f(\sigma) = \tau_{\max} - \sigma_Y, \tag{22}$$

with yielding starting when $f(\sigma) = 0$. After the onset of yielding, the Duvaut-Lions-type viscoplasticity (e.g. Simo & Hughes 1998, chapter 2.7; Andrews 2005; Duan & Day 2008) is employed to

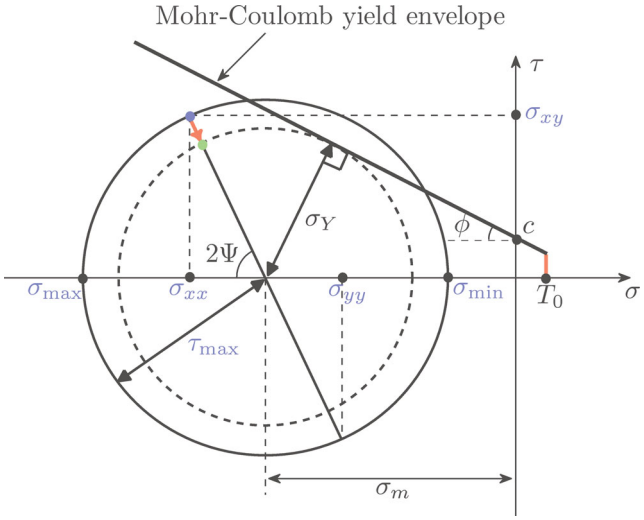

Figure 6. A schematic diagram of the off-fault Mohr–Coulomb yielding criterion, with ϕ being the internal friction angle and c denoting the rock cohesion. The solid circle describes a trial stress state that may be measured along arbitrarily oriented surfaces and the blue dot (associated with σ_{xx} and σ_{xy}) represents the stress on the plane normal to the x-coordinate of Fig. 1. The dashed circle and its interior represent the elastic regime preserving the current mean stress σ_m. The Mohr–Coulomb yield envelope is characterized by the thick black line. The yield envelope in the tensile regime is represented by the red line, with T_0 being the yielding strength under tension (see text for more details).

describe the accumulation of plastic strain through the following non-associated flow rule:

$$\dot{\varepsilon}_{ij}^p = \frac{\langle \tau_{\max} - \sigma_Y \rangle}{2\mu T_v} \frac{\tau_{ij}}{\tau_{\max}}. \tag{23}$$

Here T_v is a viscoplastic timescale over which the stress is relaxed back to the elastic domain (bounded by σ_Y), $\langle x \rangle = (x + |x|)/2$ is the ramp function (sometimes also called penalty function) defining the 'driving force' for the plastic strain as the excess distance (in proper stress space) of the maximum shear stress $\tau_{\max}$ over the yielding strength σ_Y, and $\tau_{ij} = \sigma_{ij} - (1/2)\sigma_{kk}\delta_{ij}$ (with the Einstein summation convention assumed) are the deviatoric stress components in 2-D through which plastic strain is partitioned into different components (i.e. $\dot{\varepsilon}_{ij}^p \propto \tau_{ij}$). This non-associated flow rule (with $\dot{\varepsilon}_{ij}^p$ generally not proportional to $\partial f(\sigma)/\partial \sigma_{ij}$) also implies that the mean stress σ_m does not change during each relaxation step and there is no volumetric change to the plastic strain over the bulk (i.e. $\varepsilon_{kk}^p \equiv 0$). Such rate-dependent rheology is often used as a regularization of plasticity to avoid or delay the occurrence of strain localization (such as shear band), which is strongly mesh-dependent in numerical studies (e.g. Templeton & Rice 2008; Dunham *et al.* 2011). In our study, the viscoplastic relaxation timescale T_v is set to be the P-wave traveltime over several grid points such that shear localization is effectively avoided (e.g. Andrews 2005; Duan & Day 2008).

The magnitude of the accumulated plastic strain is quantified with a scalar quantity defined as $\varepsilon_0^p = \sqrt{2\varepsilon_{ij}^p \varepsilon_{ij}^p}$ (e.g. Ben-Zion 2003, 2008). This may be called the scalar seismic potency density per unit rupture length (or just potency density). We note that the plastic strain in our study is treated as a real strain tensor reflected by the factor 2 in the denominator of eq. (23). This is similar to the well-known 'transformation strain' of Eshelby (1957) that is used in seismology (e.g. Aki & Richards 2002). Some other studies define the plastic strain using the engineering notation (e.g. Andrews 2005; Duan 2008) without the above factor 2 in eq. (23).

A geometric interpretation for the employed yielding criterion and viscoplastic rheology is shown in Fig. 6. A full description of the trial stress state is characterized by the solid Mohr circle, and is in particular described by the blue dot associated with a normal component σ_{xx} and a shear component σ_{xy} in the (σ, τ) stress space. As indicated by the fact that the solid Mohr circle is intersected by the yield envelope, the trial stress violated the yield strength and should be relaxed back towards the elastic domain. The external boundary of the elastic stress, keeping the current mean stress σ_m unchanged, is described by the dashed Mohr circle. Depending on the viscoplastic timescale T_v, the extent of stress relaxation can be different: for a perfect plasticity ($T_v = 0$), the trial stress will be relaxed exactly onto the boundary of the elastic domain, whereas for a general rate-dependent viscoplasticity ($T_v > 0$) it will be relaxed to some transition state between its trial state and the fully relaxed state characterizing the external boundary of the elastic domain. Because the relaxation is always performed along the deviatoric stress direction, a specific relaxation path for the stress components σ_{xx} and σ_{xy} is given by the red arrow, starting from the blue dot and pointing to its closest projection onto the boundary of the associated elastic domain (the green dot on the dashed Mohr circle; e.g. Simo & Hughes 1998).

The above employed Mohr–Coulomb yielding criterion is strictly appropriate only for rocks under absolute compression or partial tension (e.g. $\sigma_{\min}$ may become tensile whereas $\sigma_{\max}$ still remains compressive) loading conditions (e.g. Etheridge 1983; Hancock 1985; Jaeger *et al.* 2007), when the corresponding fracture can be treated as internal frictional sliding of mode-II shear type. Some field and laboratory observations have reported tensile microfractures (mode-I) or coexistence of both tensile and shear microfractures around the principal slip surface (e.g. Stanchits *et al.* 2006). This implies that it is more realistic to employ a yielding criterion that covers the compressive regime, the tensile regime, and the transition in between, with some attention to the fact that tensile-type yielding strength (e.g. T_0 in Fig. 6) is usually weaker than the shear-type yielding strength (e.g. Willson *et al.* 2007). However, because of the relative simplicity of the Mohr–Coulomb yielding criterion and the subsequent flow rule, we follow previous works on off-fault inelastic response and use these constitutive laws. As in previous studies, the results may be used to estimate the potential for inducing off-fault mode-I fractures (see section 3.3.1).

2.5 Numerical method and parameters

We use the 2-D spectral element code developed by Ampuero (SEM2DPACK-2.3.6, http://sourceforge.net/projects/sem2d/) to perform dynamic rupture simulations. The domain is discretized into square elements, with five Gauss-Lobatto-Legendre nodes non-uniformly distributed per element edge.

All physical quantities (constants or variables) in our numerical study are normalized so that scaling relations can be easily shown by their apparent values (e.g. Madariaga & Olsen 2002). As examples, for a self-similar expanding crack, the slip Δu is expected to scale with the stress drop $\Delta\tau$ as: $\Delta u \sim (\Delta\tau/\mu)\cdot\sqrt{L^2 - x^2}$ with μ being the shear modulus and L being the rupture distance measured from the hypocentre; the steady-state slip velocity $\Delta\dot{u}_{ss}$ far behind the rupture tip is expected to scale with $\Delta\tau$ as: $\Delta\dot{u}_{ss} \sim (\Delta\tau/\mu)\cdot c_s$ with c_s being the S-wave speed (e.g. Scholz 2002, p. 194). Reference values of some fundamental parameters are summarized in Table 1. For convenience, we convert physical quantities into dimensionless quantities for plotting the results, as summarized in Table 2.

To provide a fine resolution for simulations with and without material contrast, an average grid size $\overline{\Delta x} = (\Delta x_{\min} + \Delta x_{\max})/2 = 0.0625 L_0$ is used (with Δx being the distance between two neighbour nodes). This ensures that there are enough numerical cells to resolve the process zone size R (or R') under SWF, the critical wavelength $\lambda_{\rm cr}$ (or λ'_{cr}) under RSF, and the characteristic length scale L_0 under TWF during the nucleation stage. The time step is determined from the Courant-Friedrichs-Lewy (CFL) stability criterion:

$$\mathrm{CFL} = c_p \Delta t / \Delta x_{\min}, \tag{24}$$

with c_p being the fastest P-wave speed and $\Delta x_{\min}$ being the minimum grid size. In all simulations, CFL is fixed at 0.55.

Table 1. Material properties and employed parameters for friction laws, nucleation procedure and viscoplasticity.

Parameters	Symbols	Values
Lamé parameters (medium-1 and -2)	λ, μ	1, 1
P- and S-wave speeds (medium-1 and -2)	c_p, c_s	1.732, 1
Mass density (medium-1 and -2)	ρ	1
Poisson's ratio	ν	0.25
Static friction coefficient (SWF and RSF)	f_s	0.6
Dynamic friction coefficient (SWF)	f_d	0.1
Direct effect coefficient (RSF)	a	0.001
Evolution effect coefficient (RSF)	b	0.501
Dynamic friction coefficient (RSF)	$f_d = f_s + a - b$	0.1
Characteristic slip distance (SWF and RSF)	D_c	1
Characteristic slip velocity (RSF)	V_c	1
Characteristic length scale for nucleation (TWF)	L_0	1
Internal friction angle	ϕ	30.9638°
Time scale for viscoplastic relaxation	T_v	$0.075 L_0/c_s = 0.075$
Reference stress	σ_c	$\mu D_c/L_0 = 1$

Table 2. Convention for converting physical quantities (x) into dimensionless quantities (x') in 2-D.

Length	Time	Slip	Slip velocity	Strain	Energy	Energy rate
$l' = \frac{l}{L_0}$	$t' = \frac{t c_s}{L_0}$	$\Delta u' = \frac{\Delta u}{D_c}$	$\Delta\dot{u}' = \frac{\Delta\dot{u} L_0}{D_c c_s}$	$\varepsilon' = \frac{\varepsilon\mu}{\sigma_c}$	$E' = \frac{E}{\sigma_c D_c L_0}$	$\dot{E}' = \frac{\dot{E}}{\sigma_c D_c c_s}$

3 RESULTS

Before performing a detailed parameter-space study, we present basic simulations for crack- and pulse-like ruptures with off-fault yielding. The results are used to define various measures of quantifying the generated yielding patterns, and to examine the conservation and partition of energy during rupture propagation. An almost perfect balance among different energy components with off-fault elastic (not shown here but confirmed in our study) and elastoplastic response (Section 3.2) demonstrates that the numerical code produces reliable results.

3.1 Crack- and pulse-like ruptures with off-fault yielding

Fig. 7 presents example results for an expanding crack (under SWF) and a slip pulse (under RSF). The following parameters are used for both examples: $\sigma^0_{xx} = \sigma^0_{yy} = -4.0\sigma_c$, $\sigma^0_{xy} = 1.04\sigma_c$, $f_s = 0.6$, $f_d = 0.1$, $L_{\text{nucl}} = 90L_0$, $c = 0$. Additional parameters specific to the different friction laws used in the simulations are listed in Table 1. A Kelvin-Voigt-type viscous damping layer, which is usually added around the fault to reduce numerical oscillations, is temporarily excluded to avoid interference with the energy calculations in section 3.2, but is included in later simulations.

For the expanding crack in Figs 7(a) and (c), both the off-fault plastic yielding zone and slip profiles follow generally a self-similar pattern with increasing rupture distance (or crack half length) L. The off-fault yielding zone displays a triangular shape: its thickness T (extent in fault normal direction) scales linearly with L. All the slip profiles plotted at different time steps with equal time intervals commonly show an overall elliptical shape, with the maximum slip $d_{\max}$ in the centre proportional to L.

For the slip pulse case shown in Figs 7(b) and (d), the growth of both the off-fault yielding extent and the envelope of slip profiles saturates beyond $X \sim \pm 45L_0$. This reflects a transition from an early crack-like nucleation phase to a spontaneous pulse-like rupture, as more clearly shown by the inset for slip velocity in Fig. 7(d). The saturation for all dynamic quantities (i.e. off-fault yielding zone thickness, size of the slipping patch, maximum slip velocity and final slip at a point) seems to approach a constant level, indicating that the slip pulse beyond the transition points has evolved into a quasi-steady state.

The above results are generally similar to those obtained with off-fault yielding by Andrews (2005) for dynamic cracks and by Ben-Zion & Shi (2005) for pulse-type rupture, and follow-up simulations of these types of ruptures. As noted, the key differences between the patterns of quantities generated for the crack and pulse ruptures stem from the fact that in the former class the stress concentration continues to grow with increasing rupture size, whereas in the latter class it remains (after initial transients) approximately constant (Ben-Zion & Shi 2005).

3.2 Energy conservation and partition with off-fault yielding

As part of the code verification, energy conservation and its partition during dynamic ruptures with spontaneous generation of off-fault yielding are investigated in this section. For the modelled faulting process, the total released elastic strain energy ΔE^e_{vol} should be

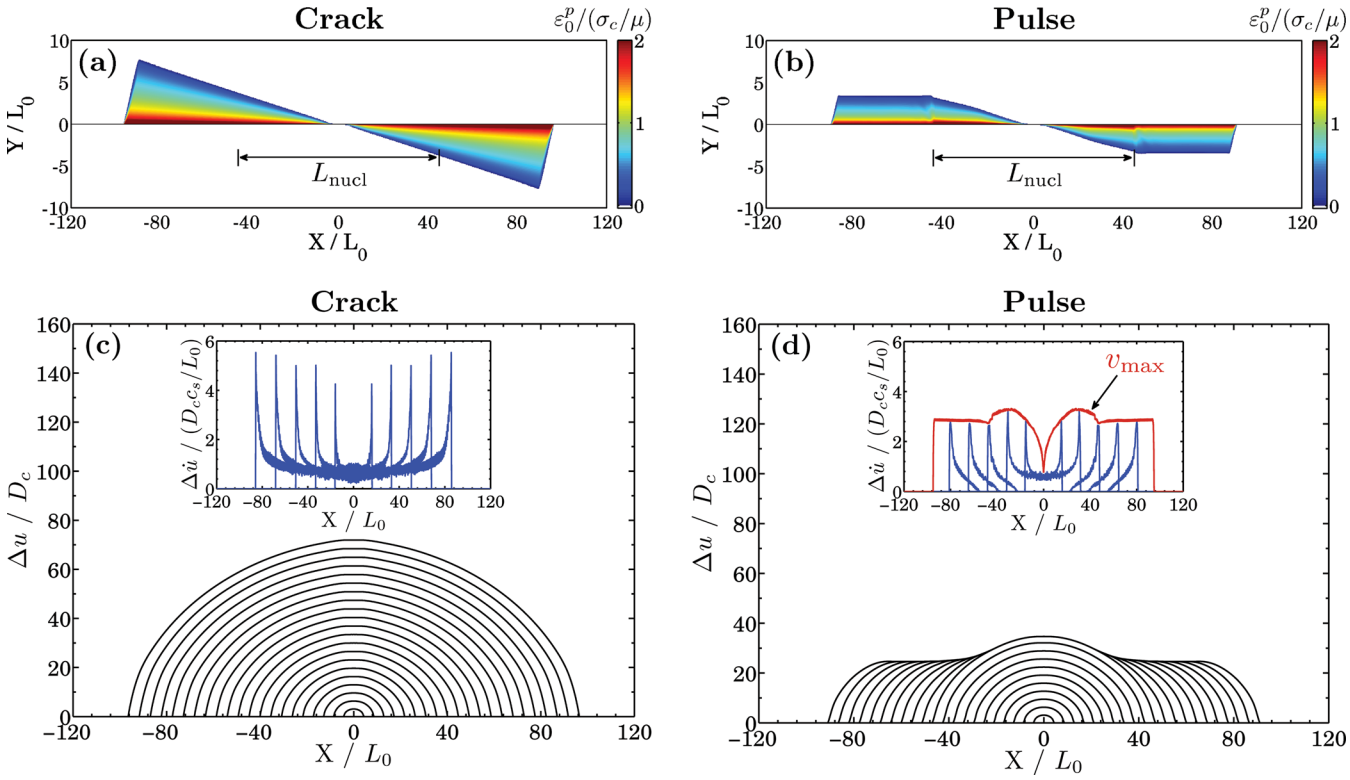

Figure 7. Plastic strain distribution for (a) crack-like rupture and (b) pulse-like rupture under same loading conditions and nucleation procedure, but with different friction laws (see text for details). The intensity of the generated plastic strain is characterized by the scalar potency density $\varepsilon^p_0 = \sqrt{2\varepsilon^p_{ij}\varepsilon^p_{ij}}$. The slip and slip velocity profiles for the crack and pulse ruptures are shown in (c) and (d). The red curve in (d) shows the maximum slip velocity profile for the pulse case.

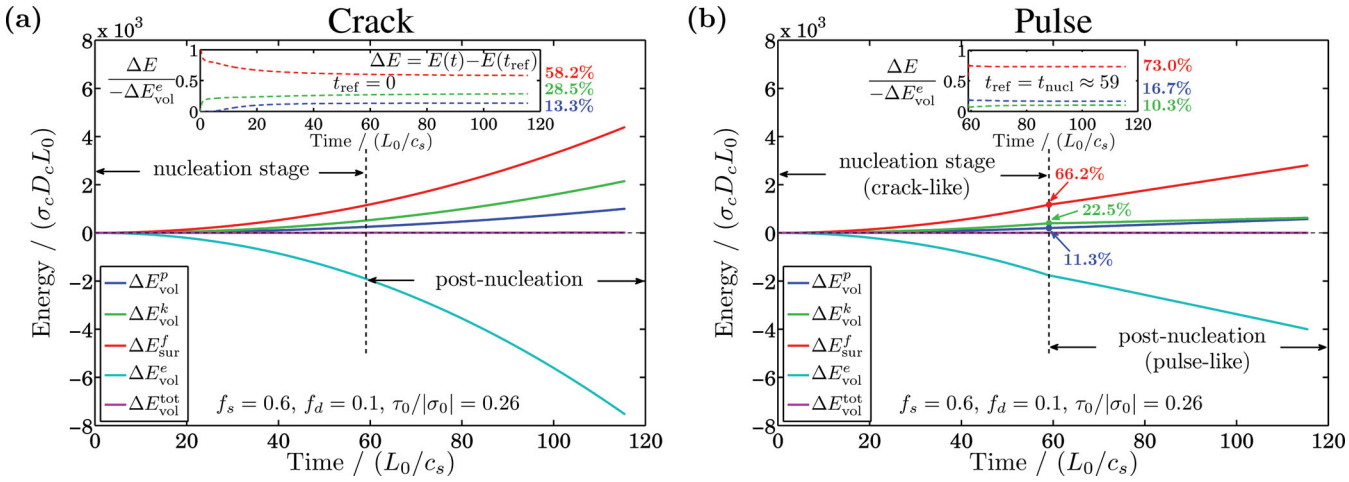

Figure 8. Various energy components versus time for (a) the crack case and (b) the pulse case of Fig. 7. $\Delta E^p_{\rm vol}$: Plastic energy dissipation, $\Delta E^k_{\rm vol}$: change of kinetic energy, $\Delta E^f_{\rm sur}$: frictional energy dissipation, $\Delta E^e_{\rm vol}$: released elastic strain energy, $\Delta E^{\rm tot}_{\rm vol}$: energy mismatch (see text for more details). The reference energy level $E(t_{\rm ref})$ for each component is usually chosen as the one at the initial time $t_{\rm ref} = 0$, but is changed to the level right after the nucleation stage $t_{\rm ref} = t_{\rm nucl} \approx 59 L_0/c_s$ when the normalized energy partition (i.e. $\Delta E/(-E^e_{\rm vol})$) is shown for the pulse case.

balanced by the change of kinetic energy $\Delta E^k_{\rm vol}$, the dissipated plastic energy $\Delta E^p_{\rm vol}$ and the dissipated frictional energy $\Delta E^f_{\rm suf}$:

$$-\Delta E^e_{\rm vol} = \Delta E^k_{\rm vol} + \Delta E^p_{\rm vol} + \Delta E^f_{\rm sur}, \tag{25}$$

where subscripts 'vol' or 'sur' indicate energy associated with a volume or along the fault surface. For our 2-D in-plane cases, all calculated energy components should be understood as energy per unit length along the antiplane direction. Calculations for various energy components are performed at a series of time steps and are stopped before the first P wave reaches the nearest absorbing boundary, so there is no energy leakage outside the domain. The various energy components appearing in eq. (25) are described in more detail below, with the understanding that all field values are functions of time.

Elastic strain energy:

$$E^e_{\rm vol} = \int_\Omega \left(\frac{\lambda}{2} I_1^2 + \mu I_2\right) {\rm d}x\, {\rm d}y, \tag{26}$$

where λ and μ are Lamé parameters, and $I_1 = \varepsilon^e_{kk}$ and $I_2 = \varepsilon^e_{ij}\varepsilon^e_{ij}$ are the first and second elastic strain invariants. The released elastic strain energy $\Delta E^e_{\rm vol}$ can be calculated by subtracting the value of the above-defined quantity at an arbitrary time t from the value at the initial time $t = 0$ when rupture is initiated.

Kinetic energy:

$$E^k_{\rm vol} = \frac{1}{2}\int_\Omega \rho \dot{u}_i \dot{u}_i \, {\rm d}x\, {\rm d}y, \tag{27}$$

where ρ is the mass density and $\dot{u}_i$ denotes the particle velocity vector. In our study, the medium is initially at quasi-static equilibrium (i.e. the reference kinetic energy $E^k_{\rm vol}$ is zero at time $t = 0$), so the change and absolute values of the kinetic energy at any time after rupture's initiation are equal.

Dissipated plastic energy:

$$\Delta E^p_{\rm vol} = \int_0^t \left[\int_\Omega \sigma_{ij}\dot{\varepsilon}^p_{ij}\, {\rm d}x\, {\rm d}y\right] {\rm d}t, \tag{28}$$

where σ_{ij} is the stress tensor and $\dot{\varepsilon}^p_{ij}$ is the incremental rate of plastic strain tensor.

Dissipated frictional energy:

$$\Delta E^f_{\rm sur} = \int_0^t \left[\int_\Sigma T_i \Delta \dot{u}_i \, {\rm d}x\right] {\rm d}t, \tag{29}$$

where T_i is the traction vector on the fault and $\Delta\dot{u}_i$ is the slip rate vector across the fault. We do not separate between the on-fault fracture energy associated with frictional weakening and pure frictional heat, but simply calculate the total dissipated energy along the fault surface (e.g. Andrews 2005; Cocco *et al.* 2006; Kanamori & Rivera 2006).

With the above definitions, we use the two examples of Fig. 7 to test the conservation and partition of energy during the propagation of the simulated dynamic ruptures. Figs 8(a) and (b) present various energy components relative to their initial levels versus time (solid curves) for the crack and pulse cases. For reference, the energy mismatch defined as $\Delta E^{\rm tot}_{\rm vol} = \Delta E^e_{\rm vol} + \Delta E^k_{\rm vol} + \Delta E^p_{\rm vol} + \Delta E^f_{\rm sur}$ is also plotted (solid purple). As seen, the purple curves in Figs 8(a) and (b) coincide closely with the background zero level (black dashed line), indicating that the total energy is almost perfectly conserved during the rupture propagation. The relative energy mismatch $\Delta E^{\rm tot}_{\rm vol}/(-\Delta E^e_{\rm vol})$ after the nucleation phase is less than 0.25 and 0.14 per cent for the crack and the pulse cases, respectively. Further calculations including a viscous damping layer can produce a negative change of $\Delta E^{\rm tot}_{\rm vol}$, since the energy loss because of damping is not included in the nominal energy balance equation. Nevertheless, with the assumed damping parameters that are used for later simulations, the results show no significant changes to $\Delta E^{\rm tot}_{\rm vol}/(-\Delta E^e_{\rm vol})$ or other relevant quantities compared to the cases without damping.

The energy calculations indicate that the expanding crack generates larger kinetic energy than the slip pulse, in agreement with Shi *et al.* (2008, 2010). This can be seen from both the absolute value of the kinetic energy (solid green) over the entire time period and the relative energy ratio $\Delta E^k_{vol}/(-\Delta E^e_{\rm vol})$ (dashed green in the inset) calculated with respect to a specified reference time $t_{\rm ref}$ (28.5 per cent for crack versus 10.3 per cent for pulse). All the energy components seem to evolve with time in a quadratic form ($\Delta E \propto t^2$) for the crack case, whereas they apparently evolve with time in a linear form ($\Delta E \propto t$) for the pulse case after the initial nucleation

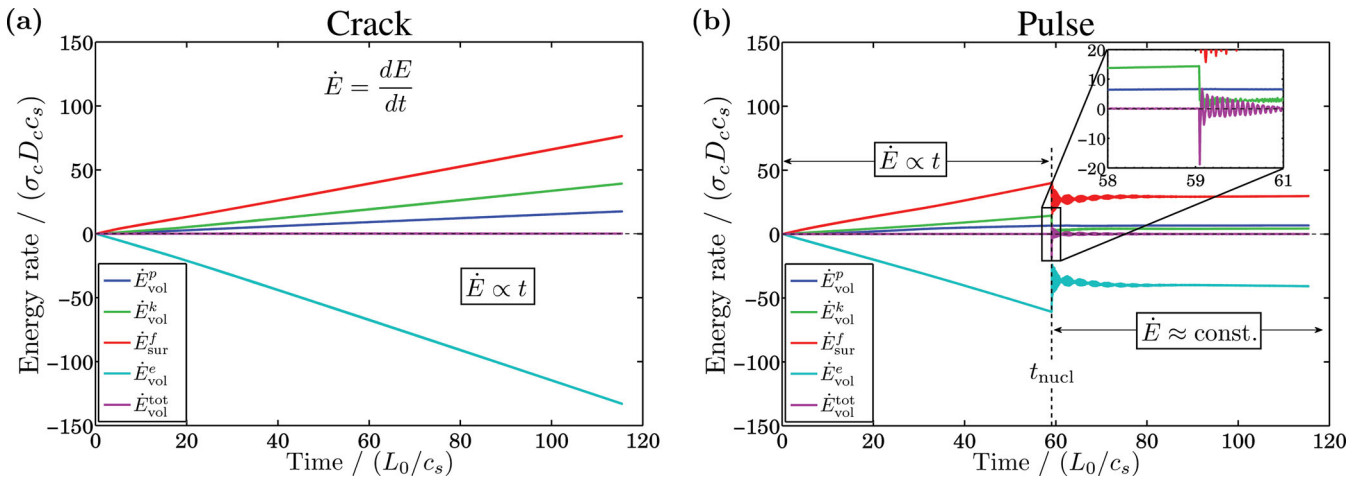

Figure 9. Energy rate versus time for (a) the crack case and (b) the pulse case of Fig. 7.

phase. These results are further confirmed by plotting the energy rate $\dot{E} = \mathrm{d}E/\mathrm{d}t$ for each component against time in Fig. 9. For the crack case (Fig. 9a), $\dot{E}$ linearly increases (with a proper sign) with time ($\dot{E} \propto t$), whereas for the pulse case (Fig. 9b), $\dot{E}$ approaches a constant level after the initial nucleation phase ($\dot{E} \approx$ const.).

The discussed energy characteristics reflect the differences in stress concentration and slipping zone size for the expanding crack and slip pulse noted earlier. Assuming the crack is expanding with a constant speed and most frictional energy dissipation along the fault goes to heat (both have been numerically confirmed in our study), we can obtain some explicit scaling relations. In such cases, the rate of dissipated frictional energy can be estimated from eq. (29) as

$$\dot{E}^f_{\rm sur} = \int_\Sigma T_i \Delta\dot{u}_i \mathrm{d}x \approx \tau_d \cdot \left(2 \int_0^{v_r t} \Delta\dot{u}\, \mathrm{d}x \right), \tag{30}$$

where τ_d is the residual shear stress (equals in magnitude to the dynamic frictional strength), and the factor 2 accounts for the fact that the crack is symmetrically expanding into two opposite directions in a 2-D in-plane configuration. Given the overall elliptical slip profile in Fig. 7(c), we can estimate the slip distribution as

$$\Delta u = \eta_1 \frac{\Delta\tau}{\mu} \sqrt{(v_r t)^2 - x^2}, \tag{31}$$

where η_1 is a dimensionless constant of order 1.09–1.5 in the sub-Rayleigh regime (Andrews 2005). The slip velocity distribution can be estimated as

$$\Delta\dot{u} = \eta_1 \frac{\Delta\tau}{\mu} \frac{v_r^2 t}{\sqrt{(v_r t)^2 - x^2}}. \tag{32}$$

Putting eq. (32) into eq. (30), we find that for the crack case $\dot{E}^f_{\rm sur}$ scales with time as

$$\dot{E}^f_{\rm sur} \approx \left(\eta_1 \pi \tau_d \frac{\Delta\tau}{\mu} v_r^2 \right) t \propto t, \tag{33}$$

where each quantity in the parentheses of eq. (33) is approximately constant with time.

In deriving eqs (31)–(33), we ignored the effects of the finite process zone and off-fault yielding, but these effects do not change our order of magnitude scaling estimate between $\dot{E}^f_{\rm sur}$ and t. Scaling relations between other energy rate components and time can be obtained from results of Andrews (2004, 2005) and Templeton (2009, chapter 4) by variable substitution between time t and crack half length L through $L \approx v_r t$.

For the pulse case, because a quasi-steady state is implied by the distribution of plastic strain (Fig. 7b) and the slip (or slip velocity) profiles (Fig. 7d), one can naturally expect that each energy rate component is invariant under time translation after the nucleation stage, at least for the time period that is studied here. In particular, the features shown in Fig. 10 (see figure caption for additional details) suggest that the slip velocity for the pulse case may be approximated by a Yoffe type function (Broberg 1999; Nielsen & Madariaga 2003):

$$\Delta\dot{u} = \eta_2 \frac{c_s \Delta\tau}{\mu} \sqrt{\frac{x + h - v_r t}{v_r t - x}}, \tag{34}$$

where h is the pulse width (Fig. 10b) and η_2 is a dimensionless function of propagation speeds at the rupture front and healing front. As implied by Fig. 10(a), both h and η_2 are expected to have constant values. Using eq. (34), we can express the energy rate $\dot{E}^f_{\rm sur}$ for the pulse case as:

$$\dot{E}^f_{\rm sur} = \int_\Sigma T_i \Delta\dot{u}_i \mathrm{d}x = 2\eta_2 \frac{c_s \Delta\tau}{\mu} \cdot \int_{v_r t - h}^{v_r t} \tau \cdot \sqrt{\frac{x + h - v_r t}{v_r t - x}} \mathrm{d}x. \tag{35}$$

As shown in Fig. 10(b), the shear traction τ has a relatively flat profile (compared to the profile for $\Delta\dot{u}$) over the major portion of the slipping zone (not close to the rupture front), suggesting that the effective value of τ in the integrand of eq. (35) may be treated as a constant $\tau_d^{\rm eff} \approx 0.26 \cdot \max\{\tau\} = 0.26\tau_s$. With this, eq. (35) can be approximately expressed as

$$\dot{E}^f_{\rm sur} \approx \eta_2 \pi h \tau_d^{\rm eff} \frac{c_s \Delta\tau}{\mu} = \text{const.} \tag{36}$$

The dynamic behaviour of the examined steady-state pulse with elastoplastic response (and related earlier results) is different from that of the self-similar subshear pulse reported by Shi *et al.* (2008) with purely elastic response. Their pulse has triangular-shaped slip profile and increasing energy rate (i.e. a growing pulse), whereas ours has almost flat slip profile beyond the nucleation zone and approximately constant energy rate (i.e. a slip pulse in quasi-steady state). We note that both steady state and growing pulses are possible rupture modes that can be produced (in addition to what is discussed above) by changing the stress condition or other model

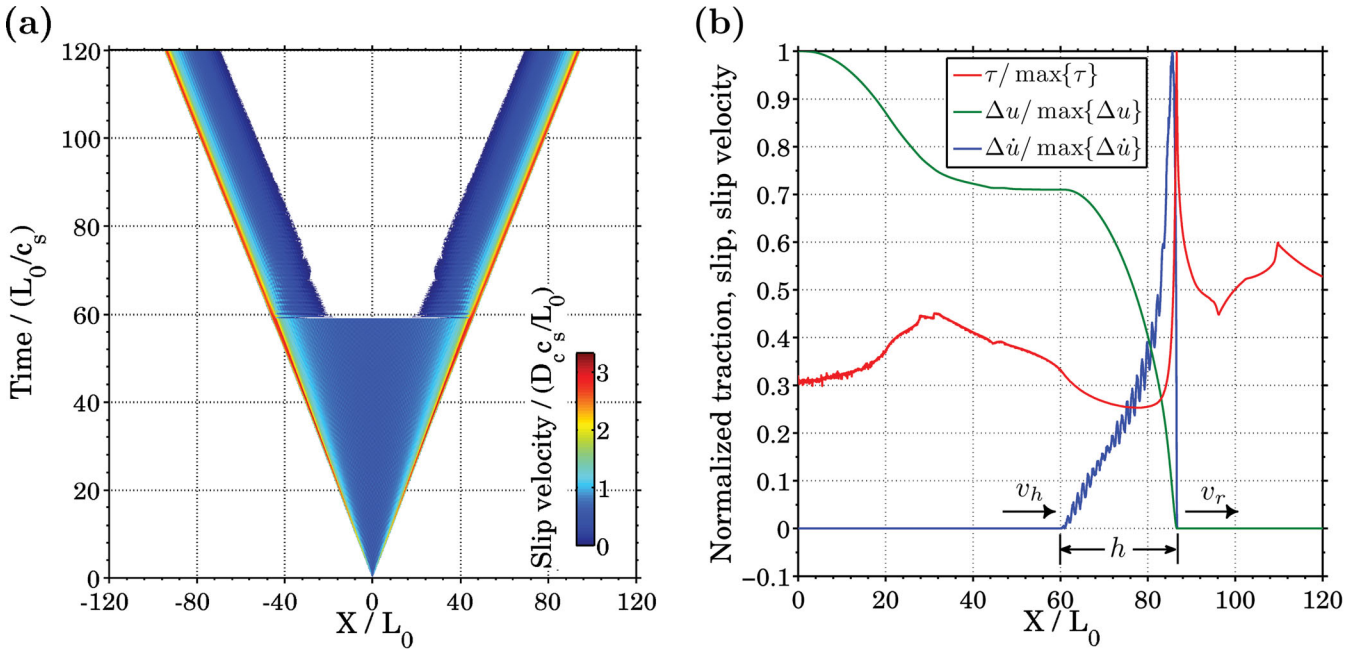

Figure 10. (a) Slip velocity as a function of space and time for the pulse case of Fig. 7(b). (b) Snapshots of normalized shear traction, slip and slip velocity (only the right half is shown because of the symmetry). The propagation speed at the rupture front and healing front are denoted by v_r and v_h, respectively, and h denotes the pulse width. Except for the bounded maximum level, $\lim_{x\to v_r t} \Delta\dot{u} \propto 1/\sqrt{v_r t - x}$ behind the rupture front and $\lim_{x\to v_r t} \tau \propto 1/\sqrt{x - v_r t}$ ahead of the rupture front. Around the healing front, $\partial u/\partial x$ is continuous, $(\partial u/\partial x)_{x=v_h t} = 0$, and $\lim_{x\to v_h t} \Delta\dot{u} \propto \sqrt{x - v_h t}$ ahead of the healing front.

parameters (e.g. Dunham *et al.* 2011). The results in Figs 8 and 9 indicate higher kinetic energy $\Delta E^k_{\rm vol}/(-\Delta E^e_{\rm vol})$ for the two rupture modes than the values calculated by Shi *et al.* (2008). This stems from the relatively large stress drops in our simulations associated with dynamic friction coefficient of 0.1. Our calculated kinetic energy is also considerably higher than the about 5 per cent or less estimates of radiated seismic energy based on seismological and laboratory data (e.g. McGarr 1999; Fulton & Rathbun 2011). This is related to the fact that the radiated seismic energy is estimated with certain observable (far field) quantities not reflecting the entire kinetic energy in the volume.

3.3 Influence of background stress orientation Ψ and rupture style

To illustrate the sensitivity of the results to some parameters and define quantities that can be useful for classifying and understanding the generated patterns, we consider cases with $\Psi = 10^\circ$ and 45°.

3.3.1 Predicted results in elastic medium

Here we use results for a purely elastic solid (no off-fault yielding) to develop connections between two aspects of mode-I and II fractures: the overall spatial distribution and the local microfracture orientation. The inferred fractures of a certain type (mode-I or -II) are predicted based on an appropriate criterion. One of the advantages of using simulations in elastic solid is that it allows considerations of many physical possibilities associated with different yielding criteria and different background stresses. In addition, the predicted results in elastic solid provide a reference for results with generation of off-fault yielding.

Following Poliakov *et al.* (2002) and Rice *et al.* (2005), we investigate properties of potential off-fault secondary fractures that may be induced by crack (Fig. 11) and pulse-like (Fig. 12) ruptures. The initial fault normal and shear stress conditions, and frictional parameters are the same as used to produce the crack and pulse cases of Fig. 7. The simulations below are done for rupture size $L = 200L_0$, and the stress component σ^0_{xx} varies in relation to the associated Ψ (eq. 4). The following criteria are used to designate likely mode-I and mode-II off-fault fractures. If $\sigma_{\rm min} \geq 0$ the yielding is assumed to be associated with mode-I fractures, whereas if $\tau_{\rm max} \geq \sigma_Y$ (with an assumption of zero rock cohesion) the yielding is designated as involving mode-II failures. Such assumptions in adopted yielding criteria might be appropriate for brittle rocks that are pre-damaged or for granular materials under low confining pressures.

When comparing the predicted patterns for crack and pulse rupture styles, we first note that the extent of the potential off-fault yielding zones (associated with either mode I or II) is larger for the expanding crack than for the slip pulse. This is again a consequence of the different stress concentrations produced by crack- and pulse-like ruptures (e.g. Ben-Zion & Shi 2005). When focusing on the same rupture style, we find that the predicted off-fault mode-II yielding zones can extend to both sides of the fault, with partition depending strongly on Ψ. On the other hand, the predicted mode-I yielding zones are primarily located on the extensional side for both low and high angles of Ψ. On the extensional side where both yielding criteria are commonly exceeded, the predicted distributions of both modes I and II fractures have a similar pattern that may be characterized by the overall orientation of several yielding zone lobes, and by the magnitude decay of the strength excess with distance from the rupture tip inside each lobe. Based on this connection, we may utilize the information on the distributed off-fault mode-II shear fractures to estimate the spatial extent (the upper bound) and the off-fault density decay of the expected mode-I tensile fractures, at least for some locations on the extensional side of the rupture.

In addition to the overall relation of spatial distribution, modes I and II fractures may also be connected by their local orientations.

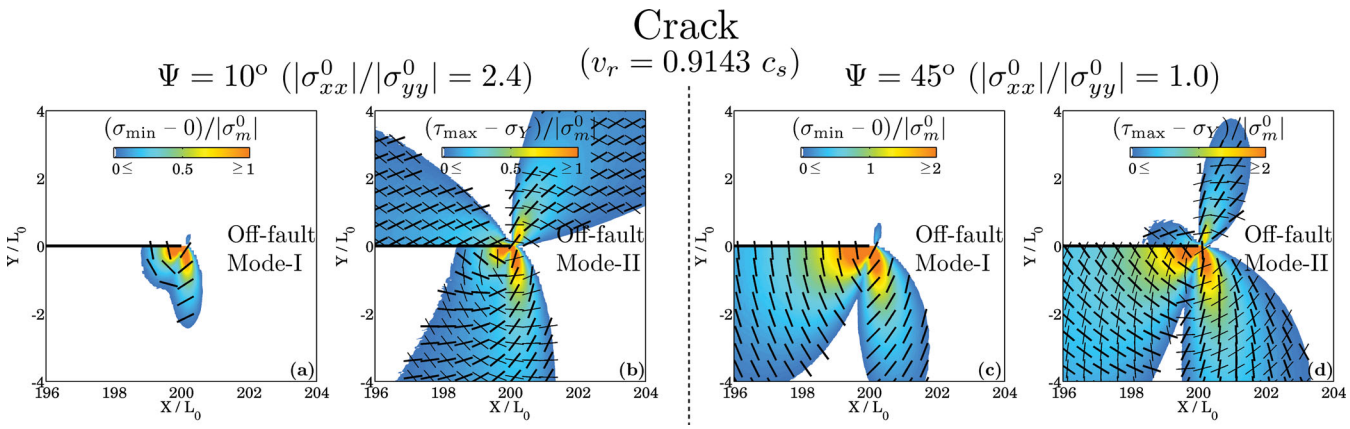

Figure 11. Predicted pattern of off-fault mode-I tensile fractures (single black bar) and mode-II shear fractures (conjugate black bars: thick and thin for the right-lateral and the left-lateral shear fractures, respectively) for cracks expanding within an elastic medium. The value of v_r indicates the instantaneous rupture speed at the time of the snapshot. $\Psi = 10^\circ$ for (a) and (b), $\Psi = 45^\circ$ for (c) and (d).

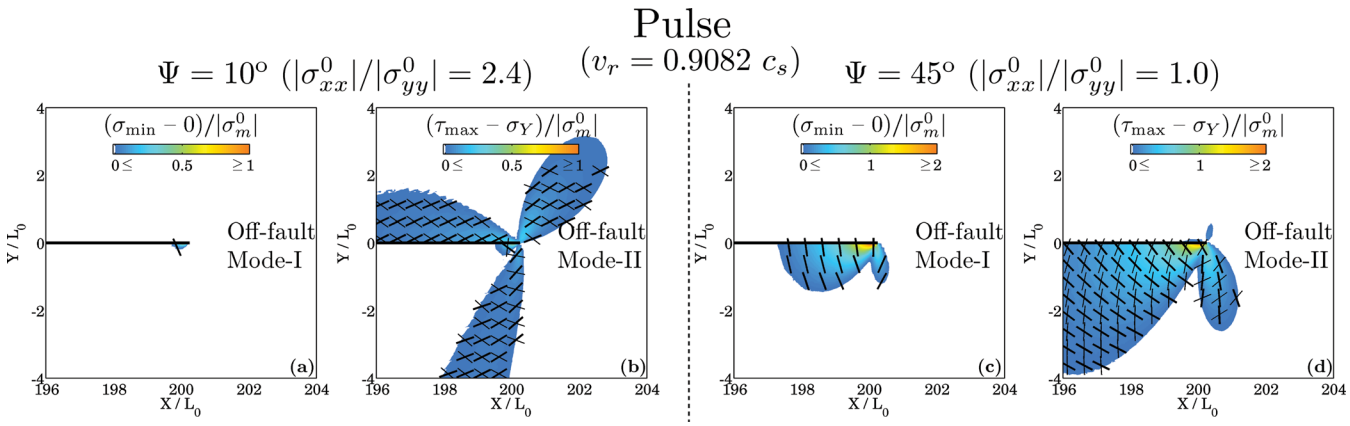

Figure 12. Similar to Fig. 11 for slip pulse under same initial stress conditions, nucleation procedure and rupture distance.

A tensile fracture is usually oriented parallel to the direction of the local maximum compressive stress $\sigma_{\max}$. A pair of conjugate shear fractures is usually generated with an angle of $\pm(\pi/4 - \phi/2)$ relative to the local direction of $\sigma_{\max}$, where ϕ is the internal friction angle (e.g. Scholz 2002; Jaeger *et al.* 2007). Therefore, with known or estimated information about the stress field, one can predict the orientation of the expected fractures. Conversely, with known information about the generated fractures, one can infer the transient stress field during the failure process. This should hold as long as the distributed fractures of a given type, tensile or shear, are individually negligible in size compared to the main fault and do not incoherently intersect (so the local stress field can be uniquely inferred) during the same failure process. Such fractures will be referred to as microfractures and are expected to reflect the local stress field. Based on this second microscopic connection, we may use later equivalent mode-II shear microfractures, through simulated distributed plastic strain, to infer the transient maximum compressive stress orientation. This should be consistent with studies modelling mode-I tensile microfractures, as long as the rupture speed and other relevant dynamic properties of the main rupture remain similar.

3.3.2 Simulation with generation of off-fault yielding

In this section we discuss and compare basic results with generation of off-fault yielding to the elastically predicted results of the previous section. Except for the difference in off-fault response (elastoplastic versus elastic), all the other conditions, procedures and parameters are similar to those of section 3.3.1.

Fig. 13 presents the distribution of the cumulative plastic strain and the equivalent plastic strain increment (through eq. 23) for crack-like ruptures that correspond to the cases of Fig. 11. As seen, the cumulative plastic strain (Figs 13a and b) is mainly located on the compressional or extensional side when Ψ is low (e.g. $\Psi = 10^\circ$) or intermediate to high (e.g. $\Psi = 45^\circ$), respectively, in agreement with previous studies (e.g. Templeton & Rice 2008; Dunham *et al.* 2011). The dependence of the location of off-fault plastic yielding zones on Ψ reflects the stress interaction between the slip-induced incremental stress field $\Delta\sigma_{ij}$ (which does not vary too much for different cases based on LEFM) and the background stress field σ^0_{ij} (which varies considerably for a change of Ψ by 35°). On the other hand, the triangular shape of the plastic yielding zones in both cases indicates that the stress concentration near the crack tip increases with rupture size regardless of whether Ψ is low or high.

Comparing the equivalent plastic strain increment (Figs 13c and d) with the predicted results for elastic medium (Fig. 11), we find that the spatial pattern of the plastic activation zone is more localized than the elastically predicted zone for cracks with a similar size. Moreover, the sense of horizontal shear can be reversed (i.e. from right lateral to left lateral) in the elastically predicted yielding zone lobes ahead of the rupture tip, whereas a reversal can be hardly seen within actual off-fault yielding regions. Finally, during generation of off-fault plastic yielding with the employed parameters, the

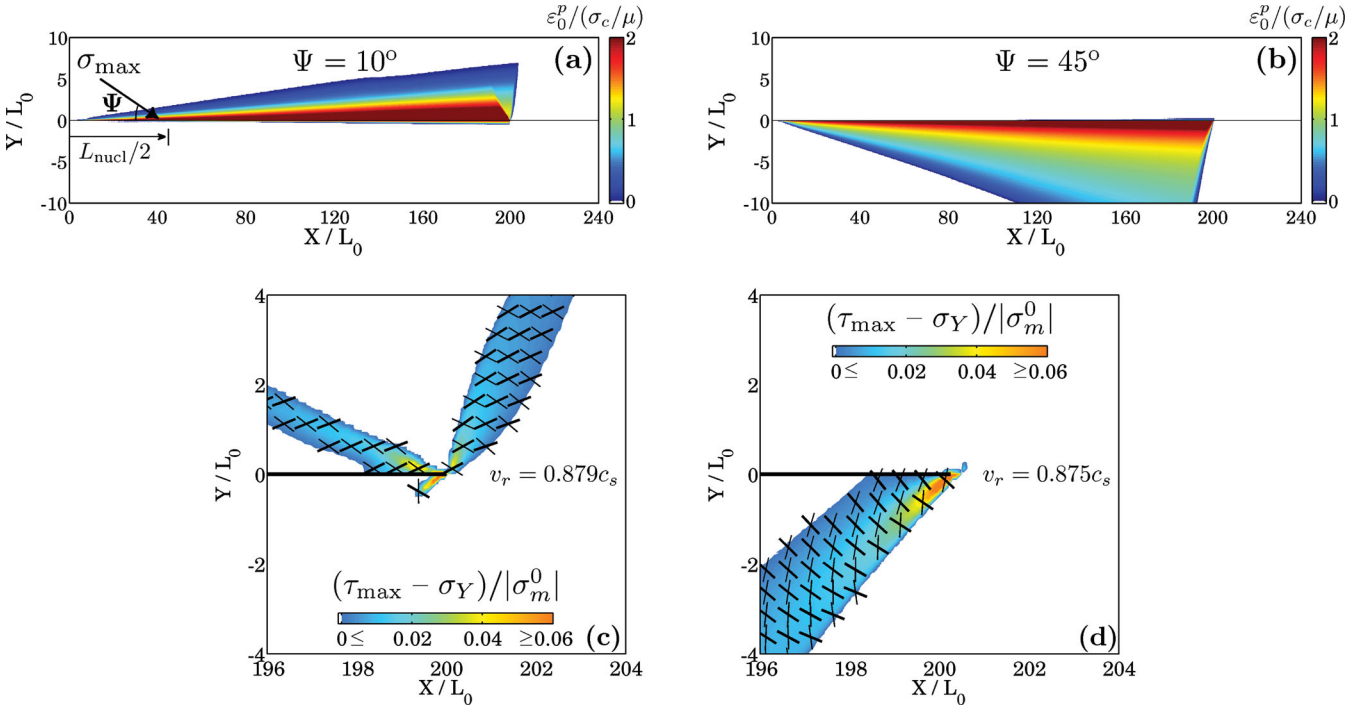

Figure 13. Distribution of (a) cumulative plastic strain for $\Psi = 10°$, (b) same as (a) for $\Psi = 45°$, (c) equivalent plastic strain increment for $\Psi = 10°$, (d) same as (c) for $\Psi = 45°$ for crack-like structures similar to the cases in Fig. 11, but with off-fault yielding.

strength excess ($\tau_{max} - \sigma_Y$) can only remain at a relatively low level (it will be exactly set at zero with a perfect rate-independent plasticity), whereas the elastically predicted strength excess can stay at a higher level. These differences may be explained by variations in rupture speed that can affect the slip-induced incremental stress field (e.g. Poliakov *et al.* 2002), and the adopted rheology, which determines how (e.g. the flow rule) and to what extent (e.g. the effective viscosity) the stress components exceeding the strength are relaxed.

In addition to these results on the distribution of plastic strain along strike or near the rupture tip, we wish to investigate local orientations of the expected microfractures in relation to the simulated plastic strain. This requires establishing connections between discretely distributed microfractures and continuously distributed plastic strain. Our modelled plastic deformation represents brittle damage zones consisting of distributed shear microfractures, whose individual size and ability to concentrate stress are negligible compared to the main rupture. The simulated plastic strain at each location can be treated as a test-particle response that reflects the transient stress field (with some modification) at the same location during the failure process. The reflected stress field is not necessarily the same as the state when plastic yielding just occurs, but should be understood as an average over the entire (short) period of the accumulation of plastic strain. The inferred stress field may be compared with inferences made with other modelling approaches.

Following the above considerations, we re-examine the results in Fig. 13 with a focus on the local orientation of the expected microfractures. To facilitate the comparison with other studies, instead of plotting pairs of conjugate shear microfractures at a point, we plot the average orientation of the inferred maximum compressive stress during the time when plastic strain is accumulated. The most favoured orientation for each expected shear microfracture can be obtained by rotating $\sim 30°$ clockwise (for a left-lateral shear) or anticlockwise (for a right-lateral shear) from the orientation of the inferred maximum compressive stress. We infer the principal stress orientation during the yielding process with a relation similar to eq. (5) as follows. Based on eq. (23), we assume the final accumulated plastic strain is proportional to the average deviatoric stress during the yielding process:

$$\varepsilon_{ij}^p \propto \overline{\tau_{ij}} = \overline{\sigma_{ij}} - (1/2)\overline{\sigma_{kk}}\delta_{ij}. \tag{37}$$

Using eq. (37) in eq. (5) and applying the model assumption that there is no volumetric change for plastic strain, we get:

$$\Phi = \frac{1}{2}\arccos\left[\frac{-\varepsilon_{xx}^p}{\sqrt{(\varepsilon_{xx}^p)^2 + (\varepsilon_{xy}^p)^2}}\right]\mathrm{sgn}\left(\varepsilon_{xy}^p\right), \tag{38}$$

where Φ is the inferred average orientation of the maximum compressive stress during the yielding process. In practice, to reduce possible numerical errors and displaying results, different plastic strain components are integrated over a spectral element (a $0.25L_0 \times 0.25L_0$ square) and the integrated quantities are used to infer the stress orientation. A colour scale is used to show the relative normal distance $d_\perp$ between the centre of off-fault elements and the fault, starting from $d_\perp = 0.375L_0$ (red) and ending at $d_\perp = 4.875L_0$ (blue).

Fig. 14 shows the inferred microfracture orientation (Φ) for the crack cases of Fig. 13. We find that the inferred orientation strongly depends on the location with respect to the hypocentre. Φ is generally shallower than Ψ in the compressional quadrant for $\Psi = 10°$, and can become steeper than Ψ in the extensional quadrant for both $\Psi = 10°$ and $\Psi = 45°$. These results are generally consistent with previous model predictions emphasizing the role of a process zone around the rupture or fault tip (e.g. Scholz *et al.* 1993; Vermilye & Scholz 1998), and also compatible with other studies on the generation of off-fault tensile microfractures (e.g. Yamashita 2000; Griffith *et al.* 2009). This general tendency of Φ being shallow in the compressional quadrant and steep in the extensional quadrant

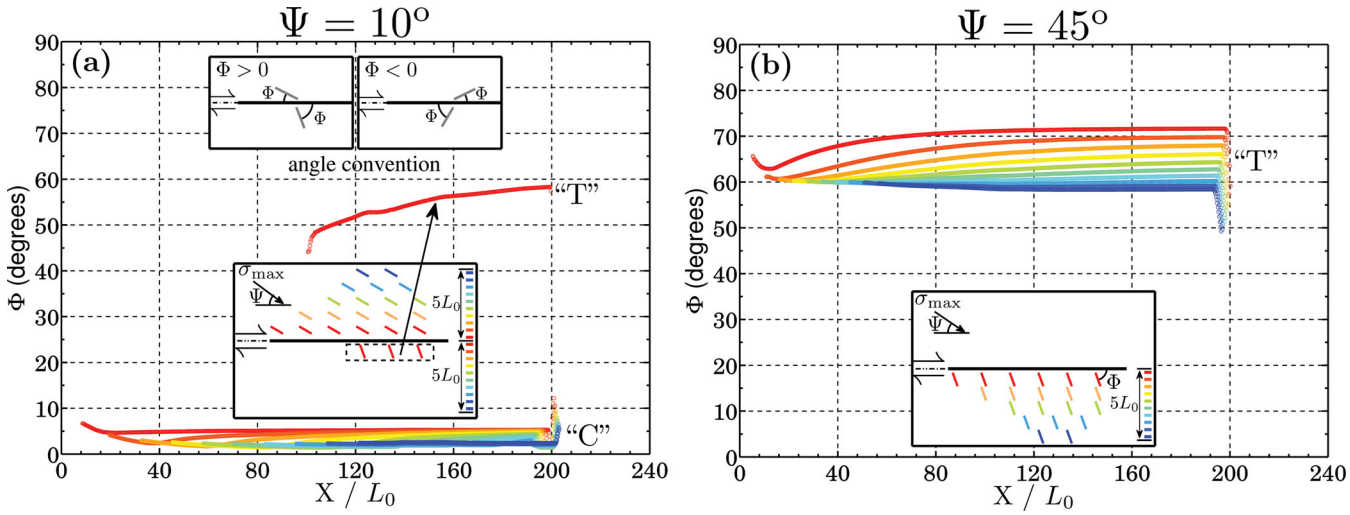

Figure 14. Inferred microfracture orientation (aligned to the direction of the maximum compressive stress σ'_{max} during failure) for the crack ruptures of Fig. 13 with (a) $\Psi = 10^\circ$ and (b) $\Psi = 45^\circ$. Φ is defined as the acute angle between the inferred orientation of σ'_{max} and the fault plane. A positive value of Φ indicates that a local horizontal right-lateral slip can be promoted by σ'_{max} whereas a negative value of Φ favours a local horizontal left-lateral slip. The colour scale represents the distance between the centre of off-fault elements and the fault (see text for details).

may reflect the characteristics of the slip-induced incremental stress field. In particular, the strong asymmetry in the distribution of Φ on the different sides of the fault may be related with the antisymmetric angular variation of the normal stress change across the fault (e.g. Freund 1990).

Another informative characteristic that has been measured in the field is the reduction of fracture density and other measures of damage intensity with distance from the fault (e.g. Wilson *et al.* 2003; Mitchell & Faulkner 2009; Savage & Brodsky 2011). To quantify this with our simulation results we examine the functional form that describes in different cases the relation between the potency density ε_0^p and normal distance from the fault. We assume ε_0^p is a good approximation of the fracture density evaluated in the field, because both quantities are correlated with the stress field around the fault. Fig. 15 shows the off-fault decay of ε_0^p with $d_\perp$ for the crack cases of Fig. 13. The colour scale indicates the sampling location along strike starting from $X = 60L_0$ (blue) and ending at $X = 180L_0$ (red). The sampling locations are neither within the nucleation zone nor too close to the rupture tip at $X = 200L_0$. At each location (given colour), data points are sampled normal to the fault on the side where plastic strain is primarily distributed. To avoid the singularity at $d_\perp = 0$ in the semi-log scale of the plot, and to focus more on off-fault (rather than on-fault) properties, we choose $d_\perp = 0.25L_0$ as the starting point for the fault normal distance.

The results in the compressional quadrant for $\Psi = 10^\circ$ (Fig. 15a) and in the extensional quadrant for $\Psi = 45^\circ$ (Fig. 15b) suggest consistently that the potency density decays logarithmically with fault normal distance in regions not close to the edge of the off-fault yielding zones where ε_0^p tapers to zero. The obtained $\varepsilon_0^p \propto -\log(d_\perp)$ form is in good agreement with other numerical simulations (e.g. Yamashita 2000) and field observations at several locations (e.g. Vermilye & Scholz 1998; Chester *et al.* 2005; Mitchell *et al.* 2011). We note that Mitchell & Faulkner (2009) and Savage & Brodsky (2011) quantified observed fault-normal decays of fracture

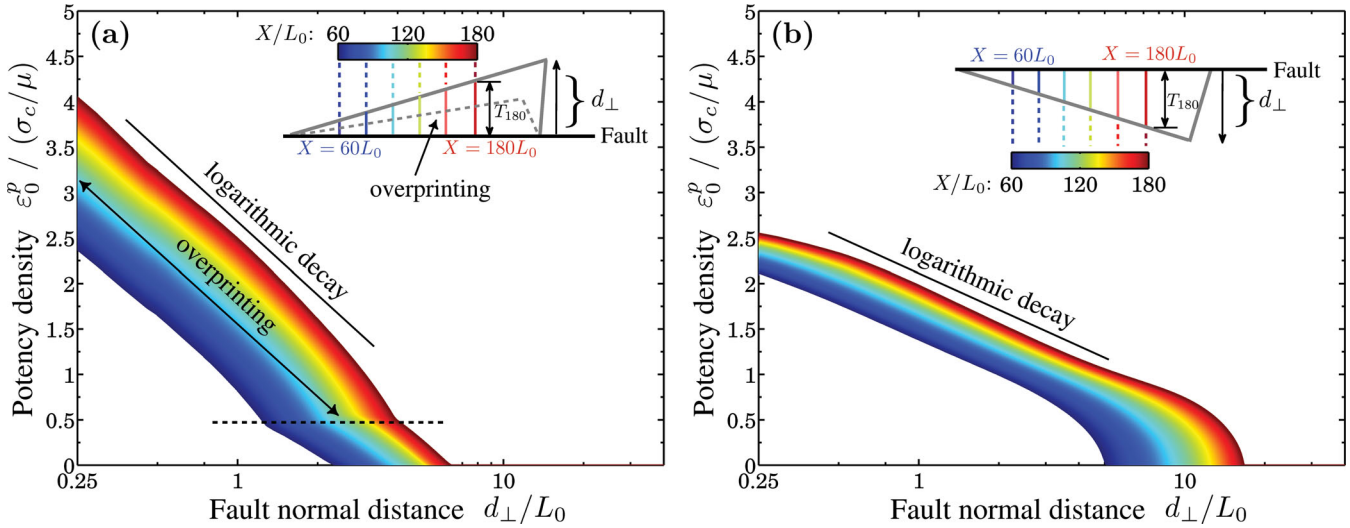

Figure 15. Decay of potency density ε_0^p with fault normal distance $d_\perp$ for the crack cases of Fig. 13. (a) $\Psi = 10^\circ$, on the compressional side. (b) $\Psi = 45^\circ$, on the extensional side. Sampling locations are linearly mapped into a colour scale, starting from $X = 60\,L_0$ (blue) and ending at $X = 180\,L_0$ (red). T_{180} represents the local thickness of off-fault yielding zone measured at the location $X = 180\,L_0$. More details are discussed in the text.

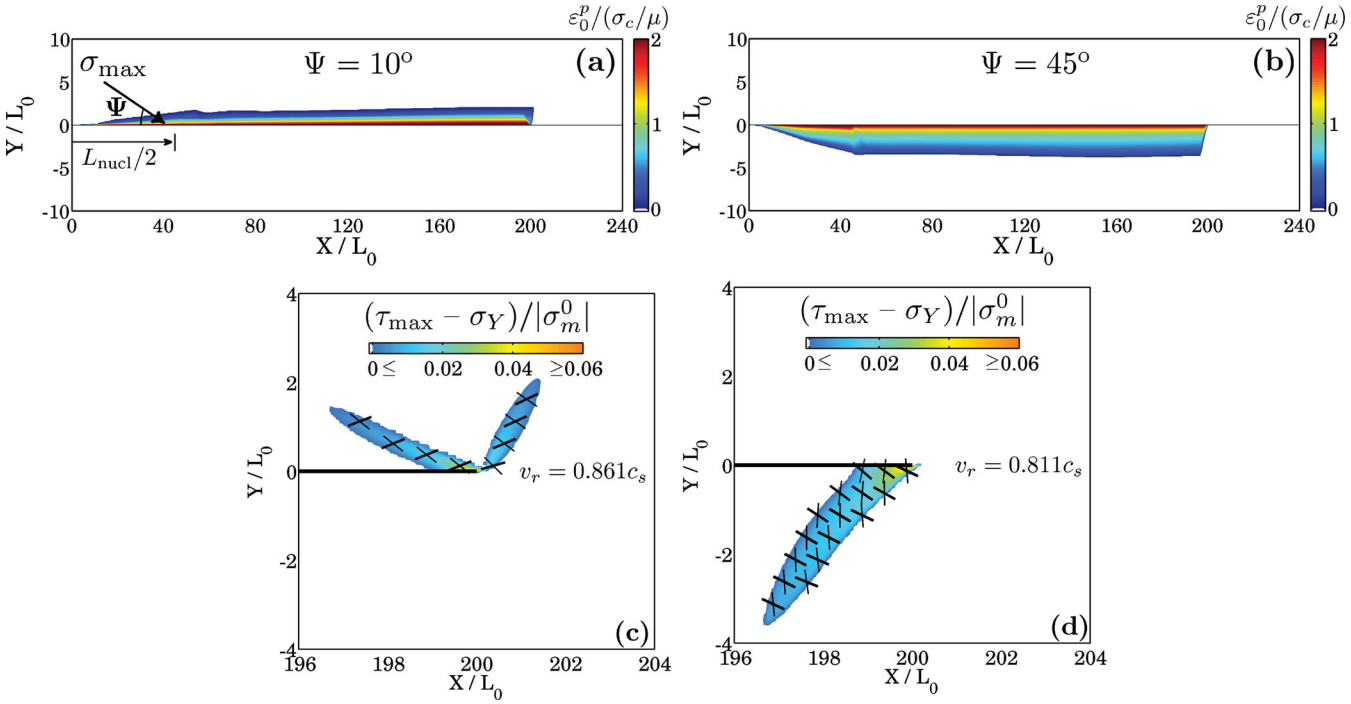

Figure 16. Distribution of (a) cumulative plastic strain for $\Psi = 10^\circ$, (b) same as (a) for $\Psi = 45^\circ$, (c) equivalent plastic strain increment for $\Psi = 10^\circ$, (d) same as (c) for $\Psi = 45^\circ$ for slip pulses similar to the cases in Fig. 12, but with off-fault yielding.

density using exponential and power law forms, respectively. However, these were not necessarily the best-fitting forms but rather preferred choices based on intended use (Mitchell & Faulkner 2009) or theoretical expectation (Savage & Brodsky 2011). The decay slope in the simulated results seems to be independent of the sampling location along strike for a given rupture case (reflected by the subparallel colour stripes), but can vary with the value of Ψ. The maximum value of ε_0^p for $\Psi = 10^\circ$ is higher than that for $\Psi = 45^\circ$at the same location. This difference may be explained by the overprinting of the two yielding lobes in the compressional quadrant around the rupture tip for $\Psi = 10^\circ$ (Fig. 13c), compared to the single yielding lobe in the extensional quadrant for $\Psi = 45^\circ$ (Fig. 13d). The possible boundary of the overprinting region for $\Psi = 10^\circ$ is indicated by the dashed grey lines in the inset of Fig. 15(a). Additional results related to the off-fault decay of ε_0^p are discussed in the follow-up companion paper.

Fig. 16 shows the distribution of the cumulative plastic strain and the equivalent plastic strain increment for pulse-like ruptures that correspond to the pulse cases of Fig. 12. As before, the cumulative plastic yielding zones have approximately constant thickness after the initial nucleation stage. The equivalent plastic activation zones (Figs 16c and d) are more confined to the rupture tip than in the crack case of Figs 13c and d. Fig. 17 shows the inferred microfracture orientation for the pulse cases of Fig. 16. Similar to the results for the crack cases (Fig. 14), the average value of Φ is lower and higher than Ψ for locations at the compressional and extensional quadrant, respectively. Because the thickness of the off-fault yielding zone is relatively narrow for pulse-type ruptures, we do not

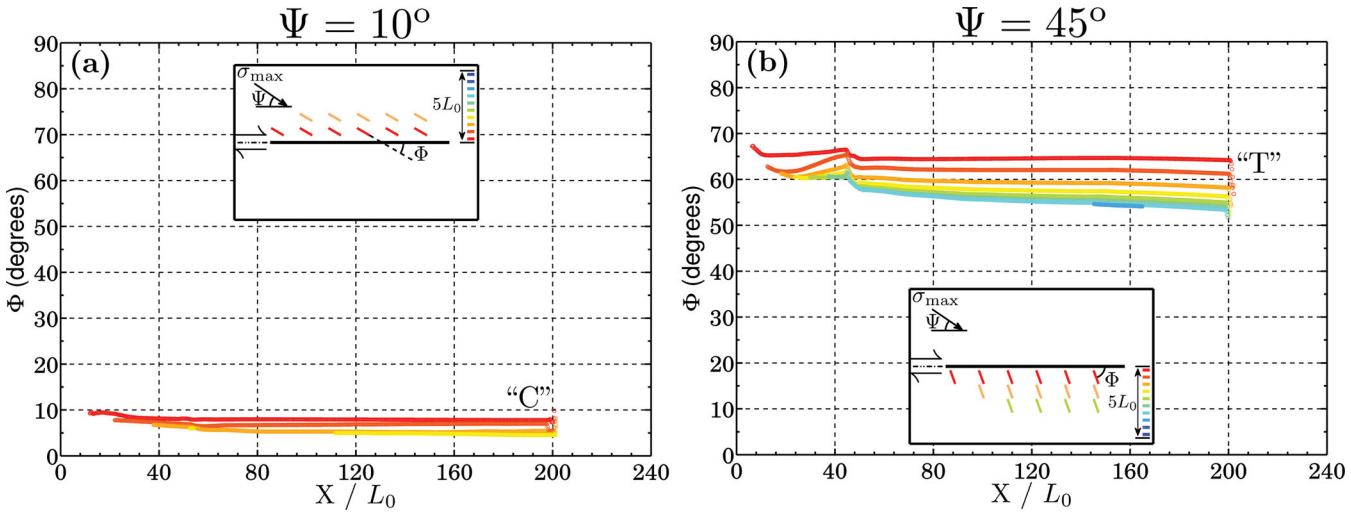

Figure 17. Inferred microfracture orientation for the pulse cases of Fig. 16.

present results on the decrease of ε_0^p with $d_\perp$ as done for the crack cases. Nevertheless, our trial functional fits to the simulated results suggest that $\varepsilon_0^p \propto -\log(d_\perp)$ also for the pulse cases.

4 DISCUSSION

We simulate in-plane dynamic ruptures on a frictional fault governed by slip-weakening and RSF laws and Mohr–Coulomb off-fault yielding. The model can be used to perform a detailed parameter-space study on various characteristics of the yielding zone generated by ruptures associated with different constitutive laws and parameters, different initial background stress, and different elastic moduli of the solids bounding the fault. Example simulations are used to demonstrate basic properties of crack and pulse ruptures and to define several measures that can help quantifying properties of off-fault yielding zones. These include the location, shape and intensity of the yielding zones, the expected orientation of modes I and II microfractures with respect to the fault, the functional decay form of yielding intensity with normal distance from the fault, and scaling relations or correlations among sets of quantities. The consistency of the numerical code is verified by the fact that energy conservation is satisfied to a very high degree.

We confirm results of previous studies that the location and shape of the off-fault yielding zones depend strongly on Ψ and the crack versus pulse mode of rupture. When Ψ is larger than about 35°, representing the likely situation for the San Andreas and other large strike-slip faults, the off-fault yielding zone produced by either crack or pulse rupture is primarily on the extensional side of the fault, in agreement with Andrews (2005), Ben-Zion & Shi (2005) and others. When Ψ is low (e.g. 15°), representing likely conditions for thrust faults, the off-fault yielding produced by either crack or pulse rupture is primarily on the compressional side, in agreement with Templeton & Rice (2008), Dunham *et al.* (2011) and others. The spatial pattern of the yielding zone increment around the rupture tip and cumulative plastic strain along the fault depend strongly on the rupture style, reflecting differences in the stress concentration around the tips of cracks and pulses with propagation distance (Ben-Zion & Shi 2005).

The energy partition among different components is influenced strongly by the rupture style under similar stress conditions and nucleation procedure. The energy rate $\dot{E}$ for various components increases linearly with time for a self-similar crack expanding at a constant rupture speed, whereas it approaches a constant level for a slip pulse under quasi-steady state propagation. These energy characteristics are consistent with the generation of the yielding zones and slip (or slip velocity) profiles for the studied rupture cases (Fig. 7). The relative energy partition $\Delta E/(-\Delta E^e_{\rm vol})$ for both rupture modes approaches in our study a constant value with time. The specific value of the constant depends on the rupture style (see the inset in Fig. 8) and may depend also on other model parameters (Shi *et al.* 2008). As expected, a considerable portion of the initial elastic strain energy is transformed during ruptures into frictional heat and plastic dissipation (although less in our calculations than estimated in other studies as noted in section 3.2), and expanding cracks produce larger kinetic energy in the bulk than slip pulses.

For both the crack- and pulse-like ruptures examined in this paper, the angle Φ of the inferred transient maximum compressive stress during failure is lower and higher than Ψ on the compressional and extensional sides, respectively. The plastic potency density ε_0^p decays logarithmically with fault normal distance $d_\perp$. These results are in good agreement with field observations (e.g. Vermilye & Scholz 1998; Mitchell *et al.* 2011) and numerical simulations of off-fault tensile microfractures (e.g. Yamashita 2000). A more complete characterization of fault yielding zones in the context of the adopted model requires a detailed parameter-space study and comparisons of predicted features with laboratory and field observations. This is done in the companion follow-up paper.

ACKNOWLEDGMENTS

We thank Massimo Cocco, an anonymous referee and Editor Xiaofei Chen for useful comments. The study was supported by the National Science Foundation (grants EAR-0944066 and EAR-0908903) and the Southern California Earthquake Center (based on NSF Cooperative Agreement EAR-0529922 and USGS Cooperative Agreement 07HQAC0026).

REFERENCES

Adams, G., 1995. Self-excited oscillations of two elastic half-spaces sliding with a constant coefficient of friction, *J. Appl. Mech.,* **62,** 867–872.

Aki, K. & Richards, P.G., 2002. *Quantitative Seismology,* 2nd edn, University Science Books, Sausalito, CA.

Ampuero, J.-P. & Ben-Zion, Y., 2008. Cracks, pulses and macroscopic asymmetry of dynamic rupture on a bimaterial interface with velocity-weakening friction, *Geophys. J. Int.,* **173,** 674–692.

Ampuero, J.-P. & Rubin, A.M., 2008. Earthquake nucleation on rate and state faults – Aging and slip laws, *J. geophys. Res.,* **113,** B01302, doi:10.1029/2007JB005082.

Ando, R. & Yamashita, T., 2007. Effects of mesoscopic-scale fault structure on dynamic earthquake ruptures: dynamic formation of geometrical complexity of earthquake faults, *J. geophys. Res.,* **112,** B09303, doi:10.1029/2006JB004612.

Andrews, D.J., 1976. Rupture velocity of plane strain shear cracks, *J. geophys. Res.,* **81,** 5679–5687.

Andrews, D.J., 1985. Dynamic plane-strain shear rupture with a slip-weakening friction law calculated by a boundary integral method, *Bull. seism. Soc. Am.,* **75**(1), 1–21.

Andrews, D.J., 2004. Rupture models with dynamically-determined breakdown displacement, *Bull. seism. Soc. Am.,* **94,** 769–775.

Andrews, D.J., 2005. Rupture dynamics with energy loss outside the slip zone, *J. geophys. Res.,* **110,** B01307, doi:10.1029/2004JB003191.

Andrews, D.J. & Ben-Zion, Y., 1997. Wrinkle-like slip pulse on a fault between different materials, *J. geophys. Res.,* **102,** 553–571.

Ben-Zion, Y., 2001. Dynamic ruptures in recent models of earthquake faults, *J. Mech. Phys. Solids,* **49,** 2209–2244.

Ben-Zion, Y., 2003. Key formulae in earthquake seismology, in *International Handbook of Earthquake and Engineering Seismology,* Part B, pp. 1857–1875, eds Lee, W.H., Kanamori, H., Jennings, P.C. & Kisslinger, C., Academic Press, Amsterdam.

Ben-Zion, Y., 2008. Collective behavior of earthquakes and faults: continuum-discrete transitions, progressive evolutionary changes, and different dynamic regimes, *Rev. Geophys.,* **46,** RG4006, doi:10.1029/2008RG000260.

Ben-Zion, Y. & Andrews, D.J., 1998. Properties and implications of dynamic rupture along a material interface, *Bull. seism. Soc. Am.,* **88,** 1085–1094.

Ben-Zion, Y. & Huang, Y., 2002. Dynamic rupture on an interface between a compliant fault zone layer and a stiffer surrounding solid, *J. geophys. Res.,* **107**(B2), 2042, doi:10.1029/2001JB000254.

Ben-Zion, Y. & Sammis, C.G., 2003. Characterization of Fault Zones, *Pure appl. Geophys.,* **160,** 677–715.

Ben-Zion, Y. & Shi, Z., 2005. Dynamic rupture on a material interface with spontaneous generation of plastic strain in the bulk, *Earth planet. Sci. Lett.,* **236,** 486–496, doi:10.1016/j.epsl.2005.03.025.

Bizzarri, A., 2010. How to promote earthquake ruptures: different nucleation strategies in a dynamic model with slip-weakening friction, *Bull. seism. Soc. Am.,* **100,** 923–940, doi:10.1785/0120090179.

Brietzke, G.B., Cochard, A. & Igel, H., 2009. Importance of bimaterial interfaces for earthquake dynamics and strong ground motion, *Geophys. J. Int.,* **178,** 921–938.

Broberg, K.B., 1999. *Cracks and Fracture,* Academic Press, New York, NY.

Caine, J.S., Evans, J.P. & Forster, C.B., 1996. Fault zone architecture and permeability structure, *Geology,* **24,** 1025–1028.

Chester, F.M., Evans, J.P. & Biegel, R.L., 1993. Internal structure and weakening mechanisms of the San Andreas fault, *J. geophys. Res.,* **98,** 771–786.

Chester, J.S., Chester, F.M. & Kronenberg, A.K., 2005. Fracture surface energy of the Punchbowl Fault, San Andreas system, *Nature,* **437,** 133–136.

Cocco, M. & Bizzarri, A., 2002. On the slip-weakening behavior of rate- and state dependent constitutive laws, *Geophys. Res. Lett.,* **29**(11), 1516, doi:10.1029/2001GL013999.

Cocco, M., Spudich, P. & Tinti, E., 2006. On the mechanical work absorbed on faults during earthquake ruptures, in *Earthquakes: Radiated Energy and the Physics of Faulting,* Geophys. Monogr. Ser. Vol. 170, pp. 237–254, eds Abercrombie, R., McGarr, A., Kanamori, H. & Di Toro, G., American Geophysical Union, Washington, DC.

Cochard, A. & Rice, J.R., 2000. Fault rupture between dissimilar materials: ill-posedness, regularization, and slip-pulse response, *J. geophys. Res.,* **105,** 25 891–25 907.

Dalguer, L.A. & Day, S.M., 2009. Asymmetric rupture of large aspect-ratio faults at bimaterial interface in 3D, *Geophys. Res. Lett.,* **36,** L23307, doi:10.1029/2009GL040303.

Dalguer, L.A., Irikura, K. & Riera, J.D., 2003. Simulation of tensile crack generation by three-dimensional dynamic shear rupture propagation during an earthquake, *J. geophys. Res.,* **108**(B3), 2144, doi:10.1029/2001JB001738.

Das, S. & Aki, K., 1977. A numerical study of two-dimensional spontaneous rupture propagation, *Geophys. J. R. astr. Soc.,* **50**(3), 643–668, doi:10.1111/j.1365-246X.1977.tb01339.x.

Day, S.M., Dalguer, L.A., Lapusta, N. & Liu, Y., 2005. Comparison of finite difference and boundary integral solutions to three-dimensional spontaneous rupture, *J. geophys. Res.,* **110,** B12307, doi:10.1029/2005JB003813.

DeDontney, N., Templeton-Barrett, E.L., Rice, J.R. & Dmowska, R., 2011. Influence of plastic deformation on bimaterial fault rupture directivity, *J. geophys. Res.,* **116,** B10312, doi:10.1029/2011JB008417.

Dieterich, J.H., 1979. Modeling of rock friction: 1. Experimental results and constitutive equations, *J. geophys. Res.,* **84,** 2161–2168.

Dieterich, J.H., 1981. Constitutive properties of faults with simulated gouge, in *Mech. Behavior Crustal Rocks,* Geophys. Monogr. Ser. Vol. 24, pp. 103–120, ed. Carter, N.L., Friedman, M., Logan, J.M. & Sterns, D.W., American Geophysical Union, Washington, DC.

Di Toro, G., Nielsen, S. & Pennacchioni, G., 2005. Earthquake rupture dynamics frozen in exhumed ancient faults, *Nature,* **436,** 1009–1012, doi:10.1038/nature03910.

Dor, O., Rockwell, T.K. & Ben-Zion, Y., 2006a. Geological observations of damage asymmetry in the structure of the San Jacinto, San Andreas and Punchbowl faults in Southern California: a possible indicator for preferred rupture propagation direction, *Pure. appl. Geophys.,* **163,** 301–349.

Dor, O., Ben-Zion, Y., Rockwell, T.K. & Brune, J.N., 2006b. Pulverized Rocks in the Mojave section of the San Andreas FZ, *Earth planet. Sci. Lett.,* **245,** 642–654, doi:10.1016/j.epsl.2006.03.034.

Dor, O., Yildirim, C., Rockwell, T.K., Ben-Zion, Y., Emre, O., Sisk, M. & Duman, T.Y., 2008. Geologic and geomorphologic asymmetry across the rupture zones of the 1943 and 1944 earthquakes on the North Anatolian Fault: possible signals for preferred earthquake propagation direction, *Geophys. J. Int.,* **173,** 483–504, doi:10.1111/j.1365-246X.2008.03709.x.

Duan, B., 2008. Asymmetric off-fault damage generated by bilateral ruptures along a bimaterial interface, *Geophys. Res. Lett.,* **35,** L14306, doi:10.1029/2008GL034797.

Duan, B. & Day, S.M., 2008. Inelastic strain distribution and seismic radiation from rupture of a fault kink, *J. geophys. Res.,* **113,** B12311, doi:10.1029/2008JB005847.

Dunham, E.M. & Rice, J.R., 2008. Earthquake slip between dissimilar poroelastic materials, *J. geophys. Res.,* **113,** B09304, doi:10.1029/2007JB005405.

Dunham, E.M., Belanger, D., Cong, L. & Kozdon, J.E., 2011. Earthquake ruptures with strongly rate-weakening friction and off-fault plasticity, Part 1: planar faults, *Bull. seism. Soc. Am.,* **101,** 2296–2307.

Eshelby, J.D., 1957. The determination of the elastic field of an ellipsoidal inclusion and related problems, *Proc. R. Soc.,* **241,** 376–396.

Etheridge, M.A., 1983. Differential stress magnitudes during regional deformation and metamorphism: upper bound imposed by tensile fracturing, *Geology,* **11,** 231–234.

Faulkner, D.R., Lewis, A.C. & Rutter, E.H., 2003. On the internal structure and mechanics of large strike-slip fault zones: field observations of the Carboneras fault in southeastern Spain, *Tectonophysics,* **367**(3–4), 235–251.

Freund, L.B., 1990. *Dynamic Fracture Mechanics,* Cambridge University Press, New York, NY.

Fulton, P.M. & Rathbun, A.P., 2011. Experimental constraints on energy partitioning during stick–slip and stable sliding within analog fault gouge, *Earth planet. Sci. Lett.,* **308,** 185–192, doi:10.1016/j.epsl.2011.05.051.

Griffith, W.A, Rosakis, A.J., Pollard, D.D. & Ko, C.-W., 2009. Dynamic rupture experiments elucidate tensile crack development during propagating earthquake ruptures, *Geology,* **37,** 795–798, doi:10.1130/G30064A.

Hancock, P.L., 1985. Brittle microtectonics: principles and practice, *J. Struct. Geol.,* **7,** 437–457.

Heaton, T.H., 1990. Evidence for and implications of self-healing pulses of slip in earthquake rupture, *Phys. Earth planet. Inter.,* **64,** 1–20.

Huang, Y. & Ampuero, J.-P., 2011. Pulse-like ruptures induced by low-velocity fault zones, *J. geophys. Res.,* **116,** B12307, doi:10.1029/2011JB008684.

Ida, Y., 1972. Cohesive force across tip of a longitudinal-shear crack and Griffiths specific surface-energy, *J. geophys. Res.,* **77,** 3796–3805.

Jaeger, J., Cook, N. & Zimmerman, R., 2007. *Fundamentals of Rock Mechanics,* 4th edn, Blackwell Publishing Ltd, Malden, MA.

Kanamori, H. & Rivera, L., 2006. Energy partitioning during an earthquake, in *Earthquakes: Radiated Energy and the Physics of Faulting,* Geophys. Monogr. Ser. Vol. 170, pp. 3–13, eds Abercrombie, R., McGarr, A., Kanamori, H. & Di Toro, G., American Geophysical Union, Washington, DC, doi:10.1029/170GM03.

Lewis, M.A, Ben-Zion, Y. & McGuire, J., 2007. Imaging the deep structure of the San Andreas Fault south of Hollister with joint analysis of fault-zone head and direct P arrivals, *Geophys. J. Int.,* **169,** 1028–1042, doi: 10.1111/j.1365-246X.2006.03319.x.

Lewis, M.A., Peng, Z., Ben-Zion, Y. & Vernon, F.L., 2005. Shallow seismic trapping structure in the San Jacinto fault zone near Anza, California, *Geophys. J. Int.,* **162,** 867–881.

Ma, S. & Andrews, D.J., 2010. Inelastic off-fault response and three-dimensional dynamics of earthquake rupture on a strike-slip fault, *J. geophys. Res.,* **115,** B04304, doi:10.1029/2009JB006382.

Madariaga, R. & Olsen, K.B., 2002. Earthquake dynamics, in *International Handbook of Earthquake and Engineering Seismology, Part A, Int.* Geophys. Ser. Vol. 81A, pp. 175–194, eds Lee, W.H.K., Kanamori, H., Jennings, P.C. & Kisslinger, C., Elsevier, New York, NY.

Marone, C., 1998. Laboratory derived friction laws and their application to seismic faulting, *Annu. Rev. Earth Planet. Sci.,* **26,** 643–696.

McGarr, A., 1999. On relating apparent stress to the stress causing earthquake fault slip, *J. geophys. Res.,* **104**(B2), 3003–3011, doi:10.1029/1998JB900083.

Mitchell, T.M. & Faulkner, D.R., 2009. The nature and origin of off-fault damage surrounding strike-slip fault zones with a wide range of displacements: a field study from the Atacama fault system, northern Chile. *J. Struct. Geol.,* **31,** 802–816.

Mitchell, T.M., Ben-Zion, Y. & Shimamoto, T., 2011. Pulverized Fault Rocks and damage asymmetry along the Arima-Takatsuki Tectonic Line, Japan, *Earth planet. Sci. Lett.,* doi:10.1016/j.epsl.2011.04.023.

Ngo, D., Huang, Y., Rosakis, A.J., Griffith, W.A. & Pollard, D.D., 2012. Off-fault tensile cracks: a link between geological fault observations, lab experiments and dynamic rupture models, *J. geophys. Res.,* **117,** B01307, doi:10.1029/2011JB008577.

Nielsen, S. & Madariaga, R., 2003. On the self-healing fracture mode, *Bull.seism. Soc. Am.,* **93,** 2375–2388.

Palmer, A.C. & Rice, J.R., 1973. Growth of slip surfaces in progressive failure of over-consolidated clay, *Proc. R. Soc.,* **332,** 527–548.

Poliakov, A.N.B., Dmowska, R. & Rice, J.R., 2002. Dynamic shear rupture interactions with fault bends and off-axis secondary faulting, *J. geophys. Res.,* **107,** doi:10.1029/2001JB000572.

Ranjith, K. & Rice, J.R., 2001. Slip dynamics at an interface between dissimilar materials, *J. Mech. Phys. Solids,* **49,** 341–361.

Rice, J.R., 1980. The mechanics of earthquake rupture, in *Physics of Earth's Interior,* pp. 555–649, eds Dzieswonski, A.M. & Boschi, E., Italian Physical Society/North Holland, Amsterdam.

Rice, J.R. & Ruina, A.L., 1983. Stability of steady frictional slipping, *J. Appl. Mech.,* **50,** 343–349.

Rice, J.R., Sammis, C.G. & Parsons, R., 2005. Off-fault secondary failure induced by a dynamic slip-pulse, *Bull. seism. Soc. Am.,* **95**(1), 109–134, doi:10.1785/0120030166.

Rousseau, C.-E. & Rosakis, A.J., 2003. On the influence of fault bends on the growth of sub-Rayleigh and intersonic dynamic shear ruptures, *J. geophys. Res.,* **108**(B9), 2411, doi:10.1029/2002JB002310.

Rousseau, C.-E. & Rosakis, A.J., 2009. Dynamic path selection along branched faults: experiments involving sub-Rayleigh and supershear ruptures, *J. geophys. Res.,* **114,** B08303, doi:10.1029/2008JB006173.

Rubin, A.M. & Ampuero, J.-P., 2007. Aftershock asymmetry on a bimaterial interface, *J. geophys. Res.,* **112,** B05307, doi:10.1029/2006JB004337.

Rudnicki, J.W. & Rice, J.R., 2006. Effective normal stress alteration due to pore pressure changes induced by dynamic slip propagation on a plane between dissimilar materials, *J. geophys. Res.,* **111,** B10308, doi:10.1029/2006JB004396.

Ruina, A.L., 1983. Slip instability and state variable friction laws, *J. geophys. Res,* **88,** 10 359–10 370.

Savage, H.M. & Brodsky, E.E., 2011. Collateral damage: evolution with displacement of fracture distribution and secondary fault strands in fault damage zones, *J. geophys. Res.,* **116,** B03405, doi:10.1029/2010JB007665.

Scholz, C.H., 2002. *The Mechanics of Earthquakes and Faulting,* 2nd edn, Cambridge University Press, New York, NY.

Scholz, C.H., Dawers, N.H., Yu, J.-Z., Anders, M.H. & Cowie, P.A., 1993. Fault growth and fault scaling laws: preliminary results, *J. geophys. Res.,* **98**(B12), 21 951–21 961, doi:10.1029/93JB01008.

Shi, Z. & Ben-Zion, Y., 2006. Dynamic rupture on a bimaterial interface governed by slip-weakening friction, *Geophys. J. Int.,* **165,** 469–484.

Shi, Z., Ben-Zion, Y. & Needleman, A., 2008. Properties of dynamic rupture and energy partition in a solid with a frictional interface, *J. Mech. Phys. Solids,* **56,** 5–24.

Shi, Z., Needleman, A. & Ben-Zion, Y., 2010. Slip modes and partitioning of energy during dynamic frictional sliding between identical elastic-viscoplastic solids, *Int. J. Fract.,* **162,** 51–67, doi: 10.1007/s10704-009-9388-6/.

Simo, J.C. & Hughes, T.J.R., 1998. *Computational Inelasticity,* Springer, New York, NY.

Stanchits, S., Vinciguerra, S. & Dresen, G., 2006. Ultrasonic velocities, acoustic emission characteristics and crack damage of basalt and granite, *Pure appl. Geophys.,* **163,** 975–993, doi:10.1007/s00024-006-0059-5.

Templeton, E.L., 2009. Effects of inelastic off-fault deformation on the dynamics of earthquake rupture and branch fault activation, *PhD thesis*. Harvard University.

Templeton, E.L. & Rice, J.R., 2008. Off-fault plasticity and earthquake rupture dynamics: 1. Dry materials or neglect of fluid pressure changes, *J. geophys. Res.,* **113,** B09306, doi:10.1029/2007JB005529.

Vermilye, J.M. & Scholz, C.H., 1998. The process zone: a microstructural view of fault growth, *J. geophys. Res.,* **103,** 12 223–12 237, doi:10.1029/98JB00957.

Viesca, R.C., Templeton, E.L. & Rice, J.R., 2008. Off-fault plasticity and earthquake rupture dynamics: 2. Effects of fluid saturation, *J. geophys. Res.,* **113,** B09307, doi:10.1029/2007JB005530.

Wechsler, N., Rockwell, T.K. & Ben-Zion, Y., 2009. Analysis of rock damage asymmetry from geomorphic signals along the trifurcation area of the San-Jacinto Fault, *Geomorphology,* **113,** 82–96, doi:10.1016/j.geomorph.2009.06.007.

Weertman, J., 1980. Unstable slippage across a fault that separates elastic media of different elastic constants, *J. geophys. Res.,* **85**(B3), 1455–1461, doi:10.1029/JB085iB03p01455.

Wilson, J.E., Chester, J.S. & Chester, F.M., 2003. Microfracture analysis of fault growth and wear processes, Punchbowl Fault, San Andreas System, California, *J. Struct. Geol.,* **25,** 1855–1873.

Willson, J.P., Lunn, R.J. & Shipton, Z.K., 2007. Simulating spatial and temporal evolution of multiple wing cracks around faults in crystalline basement rocks, *J. geophys. Res.,* **112,** B08408, doi:10.1029/2006JB004815.

Yamashita, T., 2000. Generation of microcracks by dynamic shear rupture and its effects on rupture growth and elastic wave radiation, *Geophys. J. Int.,* **143,** 395–406.